



TECHNISCHE
UNIVERSITÄT
WIEN
Vienna University of Technology

Diplomarbeit

Differentiation of ^{16}O and ^{18}O by LIBS measurement of Aluminum-Monoxide molecular emissions

AUSGEFÜHRT AM

INSTITUT FÜR CHEMISCHE TECHNOLOGIEN UND ANALYTIK

AN DER

TECHNISCHEN UNIVERSITÄT WIEN

Unter der Anleitung von

Univ.Prof. Dipl.-Ing. Dr.techn. Andreas LIMBECK

durch

Elias ELLERSDORFER BSc

Matrikelnummer 01429245

████████████████████
████████████████

Wien, Dezember 2021

Elias Ellersdorfer, BSc

Eidesstattliche Erklärung

Ich erkläre an Eides statt, dass die vorliegende Arbeit nach den anerkannten Grundsätzen für wissenschaftliche Abhandlungen von mir selbstständig erstellt wurde. Alle verwendeten Hilfsmittel, insbesondere die zugrunde gelegte Literatur, sind in dieser Arbeit genannt und aufgelistet. Die aus den Quellen wörtlich entnommenen Stellen, sind als solche kenntlich gemacht. Das Thema dieser Arbeit wurde von mir bisher weder im In- noch Ausland Beurteilenden zur Begutachtung in irgendeiner Form als Prüfungsarbeit vorgelegt. Diese Arbeit stimmt mit der von den Begutachtenden beurteilten Arbeit überein.

Wien, Dezember 2021



Elias Ellersdorfer, BSc

Abstract

A possible approach to analyze water absorption in thin-film polymers is to measure the content of oxygen introduced in the form of water. For this purpose, a differentiation between initial oxygen content (e.g. from functional groups in polymers) and oxygen resulting from water absorption by isotopic labeling is necessary. Conventional techniques to analyze water contents require bulk samples or do not allow spatially resolved analysis on thin-films.

Laser-Induced-Breakdown-Spectroscopy (LIBS) is a well-suited technique to perform spatially resolved analysis and measurements on molecular emission bands. A pronounced isotopic shift for AIO molecular emission bands in LIBS spectra is reported. So far, AIO bands have only been measured on samples, where aluminum and oxygen already are present in the form of a chemical compound, such as in Al_2O_3 . This work focused on the proof of concept regarding the generation of a laser-induced aluminum plasma (LIP) and external insertion of H_2^{18}O into the LIP. H_2^{18}O works as a source of oxygen and allows to introduce oxygen directly into the aluminum plasma. This way, both separated components are brought together and a reaction between aluminum and oxygen is forced, resulting in AIO molecular emission. Thus differentiation of generated Al^{18}O and Al^{16}O bands, resulting from natural abundant ^{16}O , can be realized. Conducted experiments included the generation of an isotopic shift in AIO emission bands and investigation of a possible correlation between introduced amounts of oxygen and signal intensities, thus investigating the possibilities for quantification.

Within this work, the adjustment of necessary experiment parameters is shown. The experiments demonstrate the possibility of external H_2^{18}O introduction direct into the LIP and thus differentiation of Al^{16}O and Al^{18}O emission bands via the isotopic shift. Varying amounts of introduced H_2^{18}O produces different signal intensities in recorded Al^{18}O bands, allowing the application of a simple calibration method.

The discussed method requires optimization and further studies to achieve application for thin-film polymer analysis.

Kurzfassung

Ein möglicher Ansatz, die Feuchtigkeitsaufnahme in Dünnschichtpolymeren zu bestimmen ist es, den Sauerstoffgehalt, der durch die Absorption von Wasser eingetragen wird, zu bestimmen. Dazu ist es notwendig, eine Unterscheidung zwischen Sauerstoff, der bereits in der Probe vorhanden ist (zB. in Form von funktionellen Gruppen in Polymeren) und dem durch Feuchtigkeitsaufnahme eingebrachten Sauerstoff, durch Isotopenmarkierung zu erreichen. Konventionelle Techniken zur Wassergehaltanalyse benötigen größere Probenmengen oder erlauben keine orts aufgelöste Analyse von Dünnschichtpolymeren.

Eine Technik, die sich gut eignet, orts aufgelöste Analyse zu betreiben, und es erlaubt, molekulare Emission zu analysieren, ist Laser Induced Breakdown Spectroscopy (LIBS). Eine ausgeprägte Verschiebung isotopischer AIO Molekülemissionsbanden ist bei LIBS Spektren gut dokumentiert. Bislang wurden derartige AIO Banden nur an Proben gemessen, in denen Aluminium und Sauerstoff bereits als Verbindung vorliegen, wie beispielsweise in Al_2O_3 . In dieser Arbeit wurde das Konzept einer Methode geprüft, in der ein Laser-induziertes Aluminiumplasma (LIP) erzeugt und externe Zufuhr von $H_2^{18}O$ in das Plasma durchgeführt werden sollte. $H_2^{18}O$ fungiert dabei als eine externe Sauerstoffquelle, die eine direkte Einführung von Sauerstoff in das Aluminiumplasma erlaubt. Dadurch sollten die beiden einzelnen Komponenten zusammengeführt und eine Reaktion zwischen Aluminium und Sauerstoff erreicht werden. Dies sollte eine Erzeugung von molekularer AIO Emission und somit eine Unterscheidung der $Al^{18}O$ Bande von der $Al^{16}O$ Bande erlauben, die sich unter der

Anwesenheit von natürlich vorkommendem ^{16}O bildet. Dabei durchgeführte Experimente hatten zum Ziel, einen derartigen Isotopenshift in AlO Emissionsbanden zu erzeugen und weiters auf eine etwaige Korrelation der eingeführten Sauerstoffgehalte und den registrierten Signalintensitäten zu untersuchen, um die Möglichkeiten einer Quantifizierung abzuschätzen.

Innerhalb dieser Arbeit wird die Einstellung von dazu notwendigen experimentellen Parametern gezeigt. Die Experimente zeigen die Möglichkeiten der externen, unmittelbaren Einführung von H_2^{18}O in das LIP und die Unterscheidung von Al^{18}O und Al^{16}O anhand des Isotopenshifts. Unterschiedliche Mengen von eingebrachtem H_2^{18}O ergeben unterschiedliche Signalintensitäten in den aufgenommenen Al^{18}O Spektren, was eine Anwendung einer einfachen Kalibrationsstrategie erlaubt.

Die behandelte Methode erfordert weitere Untersuchungen und Optimierung, um eine Anwendbarkeit für die Analyse von Dünnschichtpolymeren zu erlauben.

*Forsan et haec
olim meminisse iuvabit*

Acknowledgements

Several years have passed since the day I went to Vienna to begin my studies. Now the time has come to look back on this quest, that is now coming to an end. I will not say it was always an easy and carefree time. So I am all the more pleased to finally think back to all those wonderful moments that were granted to me here in this beautiful city and all the things that I was able to learn during this eventful journey. Undoubtedly, those pleasant hours will remain unforgettable to me.

Here at last it is now time to thank all friends and companions on this path over the last years.

First and foremost, I would like to thank my supervisor Prof. Andreas Limbeck for not only giving me the occasion to conduct this work within his working group, but also making it possible to work on a challenging project, that has never lost its charm. Every now and then, when working on this thesis and getting bogged down in pointless details, I saw him before my inner eye, rushing round the laboratory tables into the hindmost corner of the laboratory, catching me while conducting more or less important measurements and interrupting me by simply asking me what was there to report. At any time I could rely on his ideas and suggestions when knocking on his office door and asking for advice. I greatly appreciate that.

During my work many things were taught to me by "the old hands". For that reason, I would like to thank all members of the working group, for sharing their knowledge and skills with me and helping me whenever help was needed and altogether

being great colleagues. I have to express very special thanks to Maximilian Weiss and Lukas Brunnbauer, two senior assistants and genuine veterans at the LIBS, who never got tired of answering even my most annoying questions, as well as giving me valuable instructions. Their help contributed greatly to my work. Thank you.

Finally, I would like to thank my family, especially my parents. It does not happen as a matter of course that parents do support their children during their university studies. They did. Their unconditional support was evident, particularly in many phone calls, when listening patiently and laughing while I was cursing God and the world- especially before exams. At the end they were right in many situations (..I already see myself denying this in the future..). I can not express how thankful I am to you, for everything.

Contents

1	Introduction	1
2	Theoretical Background	8
2.1	Atomic Emission Spectroscopy (AES)	8
2.2	Principle of LIBS	11
2.3	Instrumental Setup	14
2.3.1	The Laser Source	15
2.3.2	The Nd:YAG Laser	16
2.3.3	Focusing and Collection Optics	19
2.3.4	Wavelength Selection and Photograph	21
2.4	Detection Components	25
2.5	Molecular LIBS of AIO	30
3	Experimental	33
3.1	LIBS Spectrometer and Experimental Setup	33
3.2	Setup for Evaporation of H ₂ ¹⁸ O	35
3.3	Materials and Sample Preparation	37
3.4	Premeasurements	38
3.5	Premeasurements on the Evaporation of Water	39
3.6	Evaporation Measurements using ETV	41
4	Results and Discussion	43
4.1	Initial Measurements and Determination of Measurement Parameters	43

4.2	Premeasurements	46
4.3	Premeasurements on the Evaporation of Water	51
4.3.1	Premeasurements on the Evaporation of H ₂ ¹⁶ O	51
4.3.2	Premeasurements on the Evaporation of H ₂ ¹⁸ O	54
4.4	Evaporation Measurements using the ETV System	59
4.5	Discussion of Problems	67
5	Conclusion and Outlook	70
	List of Figures	78
	List of Tables	79
	Appendix	80
	Bibliography	83

List of Abbreviations

AES	Atomic Emission Spectroscopy
CCD	Charge-Coupled Device
DMFC	Direct Methanol Fuel Cell
DTA	Differential Thermal Analysis
DTG	Differential Thermogravimetry
ETA	Electrothermal Analysis
ETV	Electrothermal Vaporization
FTIR	Fourier-Transform Infrared Spectroscopy
GD	Gate Delay
GW	Gate Width
ICCD	Intensified Charge-Coupled Device
ICP-OES	Inductively Coupled Plasma-Optical Emission Spectroscopy
IRMS	Isotope-Ratio-Mass-Spectrometry
LAMIS	Laser Ablation Molecular Isotopic Spectroscopy
LIBS	Laser Induced Breakdown Spectroscopy
LIP	Laser Induced Plasma
MCP	Microchannel Plate
NIR	Near-Infrared Region
NMR	Nuclear Magnetic Resonance
PLS	Partial Least Squares
PCB	Polychlorinated Biphenyls

PDA	Photodiode Array
PEMFC	Polymer Electrolyte Membrane Fuel Cell
PFCB	Perfluorocyclobutane
PI	Polyimide
PMT	Photomultiplier Tube
PSE	Periodic System of the Elements
S/N	Signal-to-Noise-Ratio
SEM-EDX	Scanning Electron Microscopy Energy Dispersive X-Ray Analysis
S-OES	Spark-Optical Emission Spectroscopy
TGA	Thermogravimetric Analysis
XPS	X-Ray Photoelectron Spectroscopy
XRF	X-Ray Fluorescence Spectroscopy
YAG	Yttrium Aluminum Garnets

1 Introduction

Oxygen is an essential element that is involved in many biological, environmental and technological processes. In biological systems oxygen occurs for example in the human metabolism as free radicals, or as molecular compounds such as peroxide species, fulfilling roles as signal molecules, or being formed within metabolic paths [1]. Reactive oxygen species are consumed in biological organisms, which is an essential property of aerobic life forms [2]. It is for this reason, that molecular oxygen can be seen as a bio-signature, that is directly related to respiration processes such as photosynthesis, allowing to metabolize nutrients by oxidation [3][4][5]. In technology oxygen plays an important role in ion conductors, or generally in metal oxides, which are often used as catalysts, ceramics, or semiconductors [6][7][8][9]. As well, oxygen is used in many technological processes as an oxidizing agent, such as steel-making processes [10][11]. However, especially in the field of material sciences, the occurrence of oxygen might cause also negative effects.

For example, the presence of oxygen in its various manifestations can influence material properties to differing extents. In this context, corrosion denotes degradation processes occurring on the surface of (primary metallic) materials. Frequent causes for this behavior are various chemical reactions with aggressive species from the environment. Molecular oxygen in the ambient air often can be seen as problematic for many engineered materials. Especially iron-based materials and alloys are prone to corrosion processes caused by oxidation at ambient conditions [12].

The best-known form of corrosion is the rusting process of iron. The non-metallic product, we are used to denoting as rust, is an undefined mixture of hydroxides and oxides of iron. Rust usually is evoked by reactive environments containing oxygen, often combined with moist atmospheres. Corrosion becomes a problem whenever the altered mechanical and chemical properties of the material render it useless. Even worse proceeded corrosion-cracking or corrosion-fatigue can lead to severe damages, entailing the risk to expose people to dangers and disasters [13]. Such immediate risk of human endangerment comes along with financial costs caused by corrosion on an industrial scale and its environmental burden [14].

The absorption of water through polymer materials presents a similar challenge. Depending on the situation, this can be a very desired property since the proton conductivity in polymer electrolyte membranes, conventionally used in Polymer Electrolyte Membrane Fuel Cells (PEMFCs) and Direct Methanol Fuel Cells (DMFCs), depends on the water absorbency of the built-in membrane [15]. To prevent damage and to extend the lifetime of such membranes, excessive uptake of water and dehydration need to be avoided. In particular, this is important, as fuel cells work under dynamic loads, due to changing power requirements, particularly in automotive applications [16][17].

Another adverse effect, caused by the uptake of water, can be observed in thin-film polymers. Substrates coated with common thin-films such as Polyimide (PI), Polychlorinated Biphenyls (PCB) or Perfluorocyclobutane (PFCB) are widely used as dielectric insulators in the microelectronic industry, due to their excellent thermal and electrical properties [18]. Water absorption under changing climatic conditions in mentioned thin-film polymers has adverse impacts on the mechanical stability of integrated polymer films. The effect is mainly expressed in the form of an anisotropic volume expansion, that leads to mechanical film stress which, in the worst case, can end up in a failure of the insulating properties of such polymer films. Notably, PI films are known to show such behavior [19][20]. As a result of water absorption,

also conductive films are formed, leading to a reduction of the insulation effect. This phenomenon may often occur at the superficial layers of polymer coatings and promotes discharge processes along the surface. Depending on the applied power, this may lead to short circuits, or worse yet, flashovers, overheating and thus material damage [21].

The above examples clearly show a high technological interest in understanding the chemism in materials that pass throughout mentioned processes. This insight is needed to generate a connection between the causing reactions on the atomic level and macroscopic manifestations, leading to mentioned unwanted properties. For gaining insights into the chemical behavior of corroded materials, X-Ray Fluorescence Spectroscopy (XRF), Optical Microscopy and Scanning Electron Microscopy Energy Dispersive X-Ray Analysis (SEM-EDX) are common techniques [22]. Other sources mention Ar⁺-sputtering X-Ray Photoelectron Spectroscopy (XPS) analysis to analyze surface layers in corroded alloys or Spark-Optical Emission Spectroscopy (S-OES) [23][24].

Routinely used techniques to determine the content of water in polymers quantitatively are Gravimetric Analysis, Thermogravimetric Analysis (TGA), Electrothermal Analysis (ETA), or Differential Thermal Analysis (DTA) and Differential Thermogravimetry (DTG). Also, gas chromatography is mentioned as a suitable technique. A very sensitive, selective technique to determine very small amounts of water can be found in Fourier-Transform Infrared Spectroscopy (FTIR) [25][26][27]. Quantification is straightforward for the Near-Infrared Region (NIR). The major advantage of FTIR lies in the non-destructive approach that also allows recovery of the sample. Other approaches are Nuclear Magnetic Resonance (NMR), chemical or electrical methods, focusing on the measurement of conductivity, resistance, dielectric properties, impedance etc. [21][26]. Moreover, mechanical studies such as determining the shear modulus can be found in the literature [28][29].

Up to here, the analytical techniques mentioned so far enable measurement of

oxygen or water content. A differentiation between the initial contents of these analytes present in the native sample and the proportion introduced from corrosion processes or humidity for example, however, is not possible. This constitutes a significant drawback of mentioned techniques. Though, this can be achieved by another technique: The use of oxygen-isotope analysis within Isotope-Ratio-Mass-Spectrometry (IRMS) measurements is well reported, enabling discrimination between ^{16}O and ^{18}O [30][31][32].

Regardless of the individual merits of this approach, IRMS does not offer the possibility of spatially resolved analysis and only provides insight into bulk properties. Both, corrosion processes and the absorption of water in thin-film polymers are issues wherein diffusion processes play a major role. This marks out why information about the spatial distribution of the analytes is necessary to improve material characteristics and wanted properties. A technique that allows collecting spatially resolved analysis is Laser Induced Breakdown Spectroscopy (LIBS). Conceptually, LIBS is a simple technique: a small amount of sample is ablated and evaporated by a laser pulse. The vapor phase is consequently heated by the laser pulse and thus converted into a plasma, with all sample components fully ionized and excited. This process requires nearly no sample preparation and allows detection of nearly every element of the Periodic System of the Elements (PSE), including oxygen [33][34].

In spatially resolved analysis, the exact position of the laser on the sample surface is linked to the gained spectral information, collected by irradiation of the sample material by the laser pulse. More accurate, it is possible to perform a scan over the sample surface by guiding the laser pulse over the sample surface and tracking the position. This allows to, for instance, plot the signal intensity of simple elements as a function of two space coordinates pixel-by-pixel. Thus, a map of the analyte can be obtained, allowing to chart single element information over the sample surface. The resulting image provides immediate information about the distribution of the analyte on the sample surface. The scanning process depends on several parameters.

Obviously, the beam diameter of the applied laser beam influences the achieved resolution, as more pixels can be recorded within a given area. Due to this sampling process, a raster image is generated, with a resolution directly depending on the spot size. Other important parameters, influencing the image quality, are the applied laser energy, pulse duration, and ambient atmospheric conditions. However, energy parameters in turn depend on the material properties of the sample. Used repetition rates lie in the range of Hz up to kHz. Spatially resolved analysis is not restricted to single element analysis. It is also possible to collect information about molecular structures. Straightforward data evaluation allows distinguishing between different spectral patterns by matching collected signal spectra to known spectral patterns in a database. However, this requires optimized statistical processes. Thereby, an identification process is possible, which is of major interest for qualitative analysis [33].

A different parameter that influences signal quality is the number of shots. Often it is not sufficient to acquire a single shot spectrum for each pixel, to receive reliable information. Usually it is necessary to acquire a higher number of shots which are then supplied as an accumulated spectrum. It must be clear though, that each shot leads to ablation of sample material. During acquisition, a crater is formed by the impinging laser pulse. Therefore, collected signals do not only result from the outmost surface of the sample material but rather represent averaged information from a layer. This must be considered when recording an image, especially when analyzing thin-layers. The last point is not a disadvantage, quite contrary, it allows a step from longitudinal resolution to depth resolution.

For many analytical issues, it is necessary to gain knowledge about the distribution of analytes in the sample material. Especially in quality control of thin-films in electronic or semiconductor industries, materials are often coated, resulting in special mechanical and electrical properties or simply for protection against corrosion processes. In many cases, coatings consist of multiple layers, often made of differ-

ent materials. In quality control and failure analysis, it is, therefore, necessary to have information about the composition and the thickness of each layer, as well as the presence or occasional absence of single layers. Even changes in the composition with depth into the bulk material can be determined, which is of interest for diffusion studies. The process of depth profiling is nothing more than the process described above for longitudinal resolution. The only difference lies in the introduction of an axial coordinate. The signal can then be plotted as a function of depth. Depth information therefore results from a functional assignment of the ablation depth to the collected signals. The ablation depth strongly depends on the applied laser energy and must be determined by other techniques (e.g. at the profilometer) [35][36].

Analyzing the ionic or atomic emission from the plasma is straightforward. Even further, atomic states recombine as time proceeds and transient molecular states are formed. Emission of light by relaxing molecular states in the plasma afterglow provides molecular information. Isotopic constituents show different, electronic, vibrational and rotational energy levels, resulting in a spectral shift. However, general-purpose spectrometers used in LIBS show resolution capacities, too weak to differ between single isotopic states. Isotopologues show pronounced and therefore accessible shifts. The influence of mass differences on molecular energy levels, more on the specified rotational and vibrational contributions, is much stronger than the influence on atomic energy states, which are solely electronic energy levels without rotational and vibrational contributions. Stark broadening and other effects do not allow to resolve isotopic shifts in LIBS spectra [37].

As mentioned above, it is necessary to generate transient molecular states, to make spectral shifts of isotopologues visible. A well-described system for the isotopic analysis of oxygen is the AIO emission between 464 and 520 nm. Molecular shifts of about 1 nm are observed for molecular emission bands of the respective ^{16}O and ^{18}O molecular species. Aluminum occurs naturally as a mononuclidic element. This

offers the advantage, that isotopic shifts arise solely as a result of oxygen isotopes. This, and the low presence of natural ^{18}O of about 0.2% [38] in the atmosphere, allow distinction between ambient oxygen and introduced ^{18}O . This way, water uptake studies in polymers e.g. become feasible. By introducing H_2^{18}O , the absorbed water can be regarded separately from oxygen, bound in functional groups (e.g. carbonyl or sulfonyl groups). Similar opportunities open up for corrosion studies or studies on minerals.

This thesis focused on the development of a LIBS-based procedure to achieve differentiation between ^{18}O and ^{16}O . For this purpose, a generation of AIO molecules in a laser-induced plasma should be attained. The resulting molecular emission in the blue-green system of the AIO emission should allow differentiation between the oxygen isotopes. Molecular emission should result in a more pronounced shift between emission bands than in atomic emission signals and thus make LIBS measurements possible. A commercially available LIBS instrument with an external spectrometer, complemented by an external Intensified Charge-Coupled Device (ICCD) detector, was used to detect emitted molecular emission of the AIO blue-green system. As samples, different oxygen-containing inorganic compounds and ^{18}O isotope enriched water were used.

2 Theoretical Background

2.1 Atomic Emission Spectroscopy (AES)

It is perhaps worthwhile, first, to take a look at the technique from which LIBS developed. Atomic spectrochemical analysis originated from various observations on elements emitting light at specific wavelengths. Considering wood fires, we visualize yellow flames caused by the prominent emission of light by ubiquitous sodium in nature. Early spectrochemical experiments tried to use such characteristic emission for analytical purposes. In initial approaches, salts in aqueous solutions were vaporized and excited in flames or glow discharge processes of gaseous states. Emitted spectra were collected and made it possible to identify present elements. Mentioned experiments were carried out at the beginning of the second half of the 19th century in the experimental laboratories of Bunsen, Kirchhoff and Fraunhofer. However, despite their phenomenological understanding of excitation and identification of various elements (foremost alkali metals, which are easy to excite and show intense emission), a deeper understanding of the processes that evoke such phenomena came only up with the development of quantum mechanics. According to Planck's law, absorption, as well as the emission of energy, happens in discrete quantized amounts. This is given by the Planck-Einstein equation (see [Equation 2.1](#))

$$E = h\nu \quad (2.1)$$

where h is a fundamental constant, known as Planck's constant. The Planck-Einstein relation provides, that atoms only absorb energy in the form of electromagnetic radiation at certain wavelengths (or frequencies). The same applies to the emission of energy in the form of light. Atomic Emission Spectroscopy (AES) is based on such spontaneous emission of light in free atoms (or ions), following a preceding excitation process. The excitation marks a process, that includes interaction between single atoms and electromagnetic radiation, leading to a change in the energy situation of (primarily valence-) electrons [39].

This requires an energy source to provide the necessary energy for the excitation process. In the first step, however, introduced energy leads to the atomization of the sample material. This marks an essential step, as atomic emission phenomena only emerge as a consequence of excited atomized matter, situated in a plasma state. Due to high thermal energy, electrons are in an energetically less favored excited state. As time passes, electrons fall back into a more favored ground state. This comes with the emission of light of a certain wavelength, which is determined by the discrete difference of energy between excited and ground state. At this point, it has to be mentioned, that not all transitions are possible. Observable transitions or "allowed" transitions follow the so called selection rules. A simplified scheme of the emission process is shown in **Figure 2.1**.

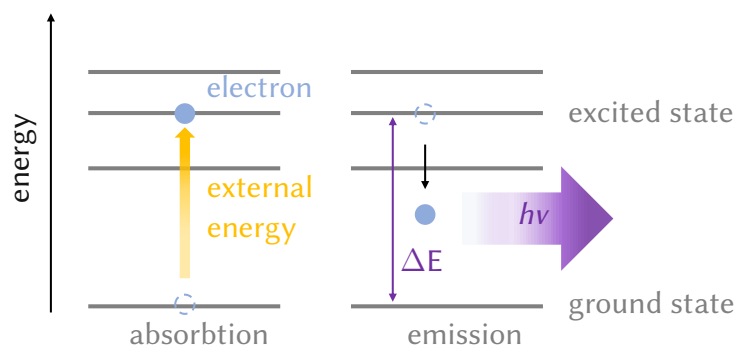


Figure 2.1: The emission process. Energy from an external source leading to an excitation of a valence electron. The relaxation of such excited states is accompanied by the emission of a photon, with a frequency ν , corresponding to the energy difference between excited state and ground state [40].

In AES flames are common energy sources, taking care of atomization and excitation. A more modern approach is Inductively Coupled Plasma-Optical Emission Spectroscopy (ICP-OES), where excitation takes place in a plasma torch. Other possible, however less common, energy sources are arcs or sparks. The energy sources, most relevant for our considerations though, are laser systems. AES nowadays is a well understood method in analytical chemistry and is routinely applied, for instance, in clinical studies such as the determination of cations (such as sodium (Na), calcium (Ca), magnesium (Mg), potassium (K), iron (Fe), zinc (Zn), copper (Cu), and selenium (Se), strontium (Sr) etc.) in human blood or serum samples [40][41][42]. Another important field of application is soil analysis. The analysis of contaminants such as heavy metals, but also nutrients and (mineral) fertilizers is reported [43]. In general, AES is a valuable tool for environmental analysis, reaching from the analysis of contaminants and pollutants such as metals in water to the analysis of plant materials [44][45][46][47]. Other applications include the analysis of oils and organic compounds or mineral acids, rare earth analysis or geochemical analysis. Furthermore, the determination of impurities in steels or alloys is mentioned as application of AES [11].

LIBS can be considered as a special application of AES, for determining the elemental composition of a wide variety of samples. It gives access to all natural occurring elements in gaseous, liquid or solid samples. During the last years, LIBS experienced a large increase in popularity. This can be attributed to the lack of sample preparation or the small quantity of ablated sample material, making LIBS a quasi-non-destructive technique. Despite the small sample consumption, LIBS shows excellent sensitivity down to the *ppm* scale. The compact and portable construction of spectrometers allows infield applications, including stand-off measurements, enabled by the integration of fiber optics. By choosing different gate delays, LIBS offers access to ionic, atomic and even molecular information. Considering typical laser frequencies, full spectral information can be collected within seconds, making LIBS attractive for applications in routine operation such as quality control, sorting,

recycling etc. Other applications range from forensics, geochemical applications, climate paleontology to archaeology and material sciences in general [48].

2.2 Principle of LIBS

The core of every LIBS instrument is a laser source. In each measurement, it provides a small laser pulse, ranging from nanosecond to femtosecond pulse duration. Most common issues in analytical chemistry deal with solid samples, therefore the easiest way is to picture solid, compact samples in the following explanations.

A laser pulse hits on a sample surface. This leads to an energy transfer to the sample matter. Material from the surface is ablated, evaporated and atomized in a first step. A vapor phase is formed near the surface, still under the influence of the enduring irradiation of the laser pulse. This leads to further heating of the vapor phase leading to consequences in two respects. Firstly, a high-temperature plasma emerges, showing a high electron density. The ablated sample material is now present in a fully ionized form. Ongoing irradiation leads to the excitation of ionized species present in the plasma. Secondly, in consequence of the ongoing heating of the laser pulse, the plasma experiences a thermal expansion (*shockwave*) at supersonic speed. Plume formation proceeds along an axis, perpendicular to the surface. At a certain point, irradiation by the laser pulse comes to an end. Now we observe a cascade of processes along a time coordinate, occurring as a result of the absent energy input. Immediately after the end of the laser pulse, the plume starts to cool down. Excited ion states relax, which comes with the emission of electromagnetic radiation. Such ion lines usually are widely broadened as a consequence of the Stark effect, which describes a splitting and shifting of ion, atom or molecular lines in a static electric field. Indeed, we experience the presence of an electric field, due to the free electrons still present in the plume. Emitted ion lines are in addition superimposed by a continuous background. Continuous background radiation again

comes as a result of accelerated free electrons. In the very first steps of the plasma cooldown, electrons are attracted by the ionized species in the plasma. Such electron capture processes finally lead to the recombination (free-bound transitions) of ionic species, forming single atoms. The associated acceleration of electrons in an external electric field leads to a continuous emission of energy (free-free transitions), usually called *Bremsstrahlung*. Schematic evolution over time of recorded LIBS spectra is shown in Figure 2.2 [34][48].

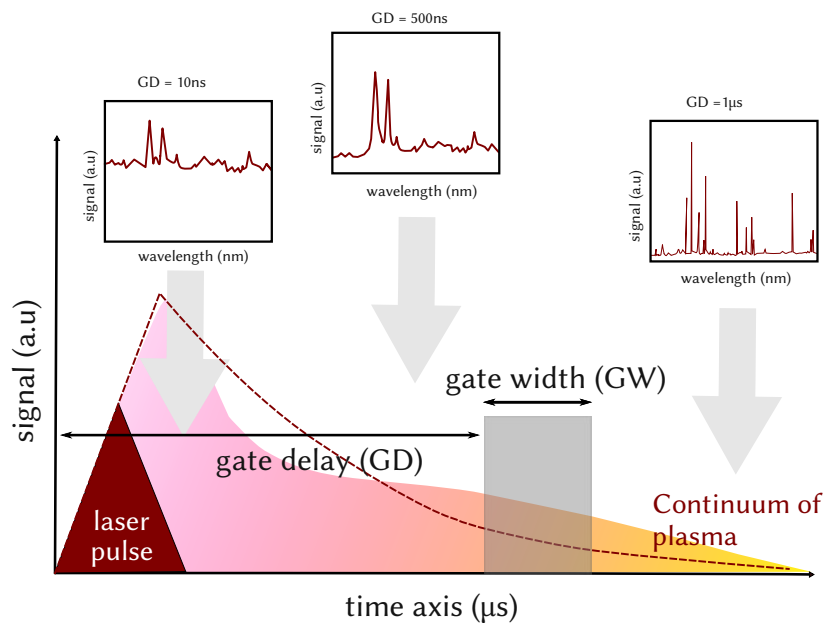


Figure 2.2: Different time regimes in the evolution of the plasma. The signal intensity reaches its maximum while the laser pulse is still enduring. Following, excited states start to collapse (breakdown). The gate delay (GD) marks the time interval between the onset of the laser pulse and the measurement. The measurement covers a certain time interval, defined by the gate width (GW). The gate width is adjusted by the ICCD detector by means of a detector gate pulse, which allows to trigger the passage of a wanted signal and to ignore unwanted signals. Short gate delays (10 ns) provide a large background and poorly resolved signals. Optimized gate delays (1 μ s) show well resolved signals but absolute signal intensities decrease. However, a higher S/N ratio is observed. Recreation from [49][50]

Within a few hundred nanoseconds electron capture and recombination processes are usually completed. Continuous background radiation decreases and atomic emission resulting from interatomic transitions become predominant in the emission

spectrum. Such atomic emission lines show a more narrowed and defined shape than mentioned ion lines. As time goes by, atoms start to recombine to transient molecular species, delivering molecules in excited states. A ternary time regime can be observed after an even longer delay of time, showing molecular emission lines. It has to be mentioned, decrease over time in signal intensity does not confine to background radiation. Signals resulting from characteristic emissions will also decrease in intensity. At first sight, this may appear self-defeating, but it must be kept in mind, that we are not interested in absolute signal intensities. It turns out, that high relative signal intensities, with low background radiation and narrow lines, are much more valuable (see [Figure 2.2](#)). To achieve this precondition an optimization of two parameters known as **Gate Delay (GD)** and **Gate Width (GW)** is mandatory [48].

In this context “gate delay” means the time interval between the onset of the laser pulse and the actual measurement. By adapting the gate delay time, the wanted type of emission (atomic, ionic, molecular emission) is chosen. Detection in ICCD type detectors takes place during a certain time window. This type of detector allows to set a gate width, and thus the application of a discrete time interval wherein emitted light is amplified and detected. The choice of the gate width allows defining a narrow time window where emitted light is collected. This is usually more relevant for measurements of ionic or atomic emission, to preserve a separation between the respective time regimes. The choice of gate width and gate delay depends on the sample and the applied instrument and preset experiment parameters, such as the laser energy. The choice of the gate delay reflects a trade-off between high absolute signal intensities and good Signal-to-Noise-Ratios (S/Ns). Optimization of gate delay and gate width is carried out at the emission band of interest. This marks a necessary process if quantification is pursued [48][33].

2.3 Instrumental Setup

In [section 2.1](#), the laser system was already discussed as the core element of a LIBS spectrometer. Now it comes upon us to discuss the other components of state-of-the-art devices. Generally, a LIBS setup consists of four basic constituents [[49](#)][[48](#)]:

- a laser source
- a focusing optics and a light collection system
- a dispersing element for wavelength separation and wavelength selection
- a detection system

Conventional spectrometers for general laboratory applications include a built-in chamber, wherein the sample is placed. Such chambers allow pressure control or flushing with different inert gases (e.g. helium or argon). For these reasons, gas-tight construction of the chamber is necessary. In most setups, chambers include a transparent window at the upper side, allowing a top-down incidence of the laser beam and impingement on the sample surface [[34](#)].

To achieve perpendicular incidence of the laser beam on the sample, an optical system is needed. The optical system usually contains a dichroic mirror, working as a "color filter". An angled arrangement of the beam path allows to filter passing laser light. Unwanted wavelengths pass the dichroic mirror, while light in a predefined range of the spectrum is reflected. This process and the beam path of a spectrometer and its components are shown in [Figure 2.3](#).

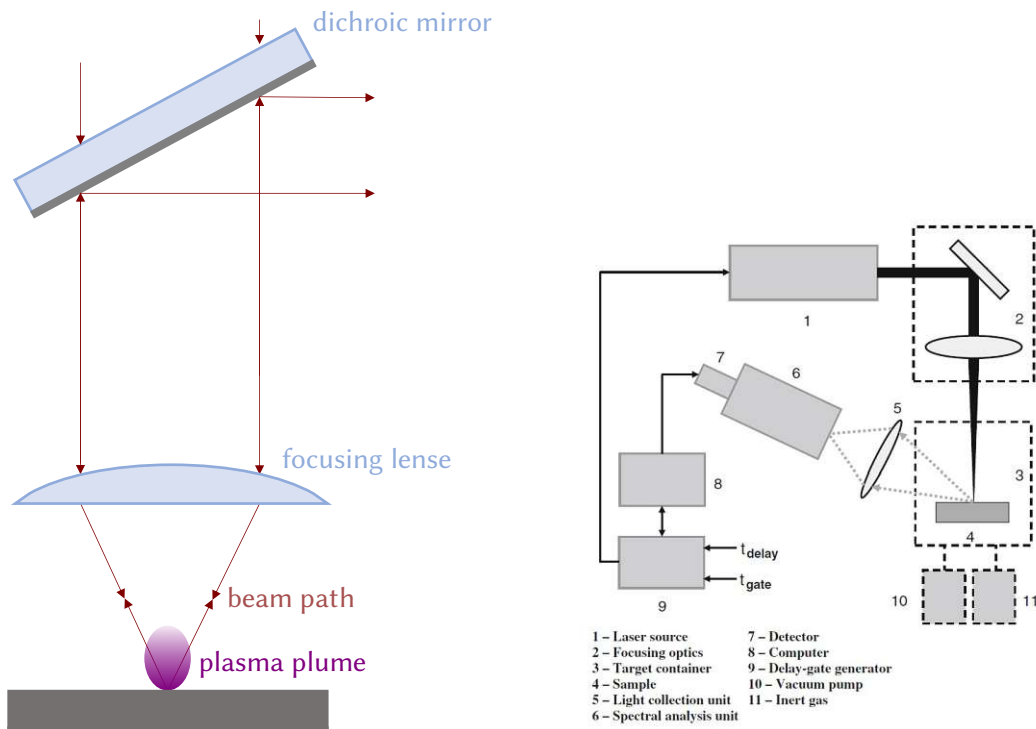


Figure 2.3: Schematic principle of a dichroic mirror (left, recreated from [33]) and experimental setup of a LIBS apparatus (right)[34].

2.3.1 The Laser Source

The laser system represents the heart of a LIBS setup. There is a large number of suitable high energy pulsed lasers. Different laser sources show differences in physical parameters such as the energy of the laser pulse, the wavelength, or the pulse duration. Accurate tuning of such parameters is important, hence small deviations largely influence the resulting plasma properties. Therefore, laser sources are often chosen with regard to the application [34].

The term **LASER** itself is the acronym for **light amplification by stimulated emission of light**. Remember section 2.1, when excitation processes were discussed. If relaxation processes take place, the energy difference between two states will be emitted in the form of electromagnetic radiation. This case is called spontaneous emission of light. The principle of laser systems however is based on the stimulated

emission of light. Thereby, relaxation is forced by an interaction between external photons and excited atoms. In contrast to spontaneous emission of light, this results in two photons, the incident one and the one resulting from the emission of energy. Both photons share the same direction, phase and wavelength, leading to an amplification of the in-phase waves [48][34].

Thus, laser sources provide high-intense, monochromatic and coherent light. The laser intensity is a physical quantity, given as a power per area. For LIBS experiments, however, we are interested in power impinging on the sample surface. This intensity depends on the cross-section between laser and surface, mainly determined by the spot size of the laser beam and the involved focusing optics. Smaller spot sizes deliver higher intensities. Common spot sizes lie in the range of around ten up to some hundred micrometers. Such small spot sizes come as a direct result of the high directionality of laser light [34].

2.3.2 The Nd:YAG Laser

An extensive range of optional laser sources is deployed in LIBS experiments. However, nowadays LIBS devices preferably use Q-switched Nd:YAG solid-state lasers. Such lasers are characterized by their comparable easy handling, their high narrow laser pulses and their high intensity. A further advantage lies in the smart design of Nd:YAG lasers, allowing compact and portable instrument design and therefore in-field applications. The fundamental wavelength of 1064 nm can be shifted to different wavelengths by frequency multiplication. Such a down-conversion to shorter wavelengths is achieved by passive harmonic generation techniques under the application of nonlinear crystals (such as quartz crystals). Modern nonlinear optics contain beta-barium borate or potassium dihydrogen phosphate crystals. Such crystals generate a multiple photon absorption, leading to excitation onto a virtual level. Relaxation leads to the emission of one photon, but with half of the initial wavelength.

This way, wavelengths of 532, 354.7 and 266 nm are achieved [48][51].

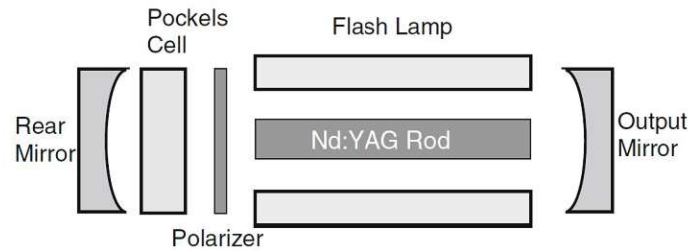


Figure 2.4: Schematic layout of a Nd:YAG laser. A flashlight is implemented, working as an optical pump [34].

Figure 2.4 shows the construction of a typical solid-state laser. A water-cooled active medium is located between two parallel arranged mirrors. One mirror works as a half mirror, showing partial light-transmissive properties for a certain wavelength. A built-in flashlight (mainly krypton (Kr) or xenon (Xe) flashlights or a diode) is installed near the active medium and allows to reach a state characterized by a population inversion. This marks a state, where the number of excited states prevails the number of ground states. In other words, there is a higher probability for higher energy levels to be occupied, than for ground state energy levels. Energy must be "pumped" to reach such a state. It must be noted, that the pumping process has to work with a different quantum mechanical transition than used in the active medium. Otherwise, a triggering of the stimulated emission would be permanently caused by the flashlight. The pumping process can also be achieved by electrical pumps. Photons resulting from spontaneous emission are reflected between the two mirrors (the resonator). The propagation of photons through the rod leads to successive stimulated emission of photons along an optical axis which is normal to the mirrors. A cascade of emissions and stimulations is observed. Photons emitted in other directions usually do not lead to the emission of light. The semi-transmissive mirror only reflects a certain wavelength, leading to a high monochromaticity and a high amplification of the light [34][48]. A typical setup of a flashlight pumped (a)

and a diode pumped (b) Nd:YAG laser is shown in Figure 2.5.

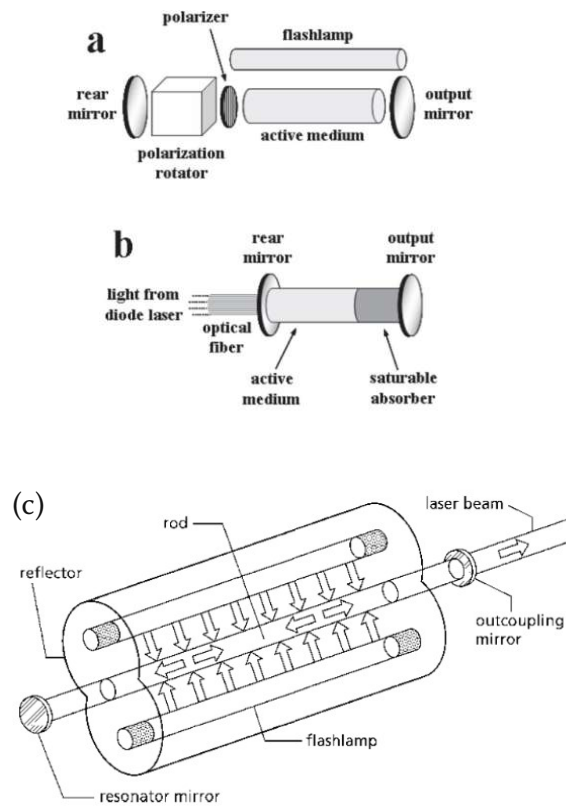


Figure 2.5: Drawing of an (a) (c) flashlamp pumped, (b) diode pumped Nd:YAG Laser [48][33].

Nd:YAG Lasers consist of Yttrium Aluminum Garnets (YAG) doped with Nd^{3+} ions. The doping with Nd ions allows emission at four levels, with corresponding wavelengths at 946, 1046, 1123 and 1319 nm [52] [34]. The most important transition for conventional Nd:YAG lasers results in emission at a wavelength of 1064 nm. YAG are very popular materials in the optical industry, due to their excellent material properties and their good thermal conductivity. The structure shows good qualities when it comes to different temperature ranges and does not show grave changes in isotropy or optical characteristics. To obtain narrow laser pulses with high intensity, a variable attenuator is installed inside the resonator. This attenuator contains a waveplate, a pockets cell and a polarizer and works as a blockage, preventing the depletion of the higher energy level. This leads to a drastic increase in the amount of

stored energy in the active medium. At some point, the population inversion reaches a maximum. The Q-switch is opened which leads to a narrow, high energy laser pulse in the nanosecond regime [34]. A Q-switch implementation is demonstrated in Figure 2.5 (a).

2.3.3 Focusing and Collection Optics

In subsection 2.3.2, we have seen the principle of conventional laser sources implemented in LIBS apparatuses. Nevertheless, Nd:YAG lasers still are incapable of providing enough irradiance to generate a qualitative sufficient plasma during interaction with the sample. By application of a focusing system, the beam diameter can be focused to a narrow spot. Optical systems allow the guidance of the laser beam onto the sample and subsequently collect the emitted radiation and further direct it to a spectrometer (wavelength selector).

To increase the irradiance, in general, spherical or cylindrical lens systems are applied. We already discussed the most conventional optical configuration, where a laser is directed perpendicularly onto the sample. In this arrangement, at least two lenses are applied. One lens is implemented to focus the laser radiation. For spatially resolved measurements short focal lenses are preferred, to allow localized plasma ignition. The second lens works as a collection optics and is placed on an axis shifted relatively to the incident laser beam. This way collected emitted radiation is guided to a wavelength selector [48][34].

Other components include dichroic mirrors, pierced mirrors, different kinds of prisms and microscope or telescope optics (mostly for stand-off applications). Latter allow more precise focus on the sample surface, which results in enhanced irradiance and thus a better plasma formation. In general, it can be stated, that smaller spot sizes are accompanied by better resolution, as smaller areas can be ablated. Although a more complex design is required, collection of the emitted radiation can

also be made on an axis coinciding with the axis of the laser beam. In such a setup, an intermediary dichroic or a pierced mirror is installed. Pierced mirrors contain a hole, enabling the incident beam to pass. Emitted light from the plasma is collected by the mirrored side and directed to the collecting lens. If a dichroic mirror is applied, the principle is basically the same, with the difference, that no hole is needed. This principle uses the property of a half mirror. Installed dichroic mirrors, therefore, have to be highly reflective at the operating wavelength of the laser but also highly transparent for the wavelength range of the emitted light. Dichroic setups show attractive features for two laser applications or double pulse excitation and are mostly used in such experiments [48].

Another important component that has to be discussed are optical fibers. Their application covers the direction of laser light and the collection of emitted radiation. This works in tandem with previously mentioned optics.

Often such fibers work as transport mediums between collecting lens and wavelength selection. Applications as laser guides are mentioned less often. To guide emitted light to the entrance of an external spectrometer, a special collection optic is needed. The emitted light needs to be collimated and focused directly in the fiber cable, which can be achieved by a special arrangement of two suitable lenses. The emitted light is collected by the fiber and guided directly to the entrance of the wavelength selection [34][48].

2.3.4 Wavelength Selection and Photograph

The requirements for high resolution dispersing systems can be summarized by two points:

- covering a broad spectral width
- the resolving power, a parameter which is defined by the minimum separation in terms of wavelengths at which two spectral features can be distinguished (see Equation 2.2).

$$R = \frac{\lambda}{\Delta\lambda} \quad (2.2)$$

$\Delta\lambda$ is defined as the smallest resolvable difference in wavelength at a certain wavelength λ . R is a common parameter to describe the resolution of optical systems and depends on the choice of dispersing elements or device properties such as slit sizes, focal lengths etc. There are two common dispersing elements [34].

The most commonly used dispersing elements in spectrometers are **gratings**. Such components are special substrates (such as special grinded crystals or also wire arrangements) containing a periodical structure, capable of bending light. The structure usually consists of parallel, line type grooves or bars on a reflective surface. Light hitting on a grating is consecutively reflected. The reflected light shows either constructive or destructive interference at different angles, resulting from a phase shift in the period caused by the diffraction. Destructive phenomena will be neglected as we are only interested in constructive interference achieving, monochromatic, separated components from a polychromatic source. This behavior is described by the interference condition (Equation 2.3)

$$d(\sin\alpha_1 + \sin\alpha_2) = n \cdot \lambda \quad (2.3)$$

where n is the order of diffraction and d is the grating period. The resolving power can be described by [Equation 2.4](#)

$$R = N \cdot n \quad (2.4)$$

where N is the number of adjacent grooves in the grating. Therefore, better resolution is obtained by finer gratings. Another important quantity is the diffraction efficiency, given as the percentage of the incident light, bent into a specific order of diffraction. The diffraction efficiency depends on the angle of incidence and the shape of the grating, the refractive properties of the reflective coating and the blaze angle. Latter is defined as the angle between the grating plane and the longer side of the tooth-shaped grooves. Blaze grooves show a maximum diffraction efficiency for a certain order of diffraction, whereas the diffraction is minimized for other orders (especially for the zeroth-order). A schematic drawing of the grating can be seen in [Figure 2.6 \[34\]](#).

Optical **dispersive prisms** represent the other known type of dispersing elements. Such prisms enable a constant deflection of light. By combining a dispersive prism with an aperture slit, selection of a specific wavelength is possible. The selection of different wavelengths becomes feasible, by turning the prism. A very popular optical prism is an optical prism with a triangular cross-section. Other geometries are described for different applications. Dispersive prisms become increasingly outdated, as gratings show better diffractive properties and are cheaper.

The use of grating-based wavelength selectors comes with a disadvantage. This type of spectrometer allows dispersing of only a small spectral window of wavelengths with high resolution. To cover larger ranges means to lower the highest possible resolution in the recorded spectrum. Usually, this problem is solved by combination of multiple grating-based spectrographs, with different selectable spectral ranges and different spectral resolutions. This allows, to enlarge the covered spectral

region at highest possible resolution [48].

Proven grating based spectrometers in LIBS experiments are Czerny-Turner monochromators, which are well-known designs used in AES over many decades. As shown in Figure 2.6, the collected radiation passes an entrance slit and strikes a concave mirror. The mirror works as a collimator and reflects the beam onto a plane grating, enabling dispersion of spectral components of the collected emission. In consequence, spectral components of different wavelengths are split up and leave the grating at different diffraction angles. The dispersed light is directed onto a second concave mirror where the beam is focused and guided onto a detector plane. Czerny-Turner spectrographs enjoy an excellent reputation in LIBS experiments and are most often installed in LIBS spectrometers [34][48].

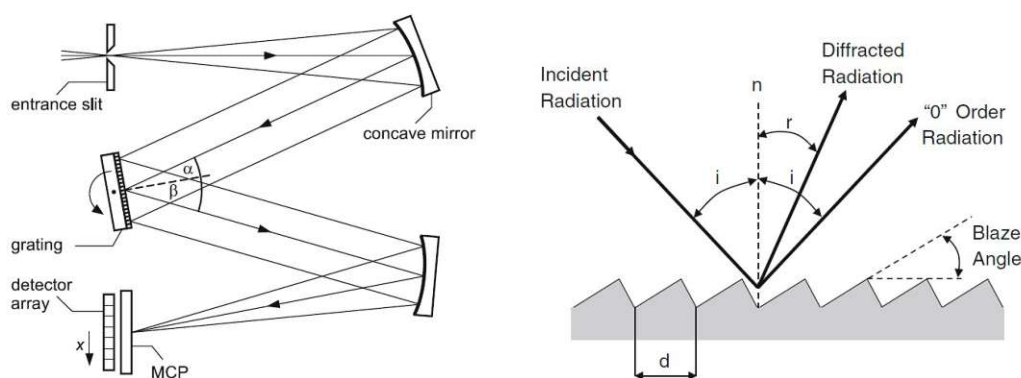


Figure 2.6: Wavelength selection in the Czerny-Turner arrangement (left) [33] and schematic drawing of a grating (right). Dispersed light beams leave the grating at different angles. The Blaze-angle is marked in an extension axis of a grating-tooth [34].

In recent times echelle spectrographs, a different type of wavelength selector, enjoyed increasing popularity in LIBS experiments. The echelle arrangement and beam path are shown in Figure 2.7.

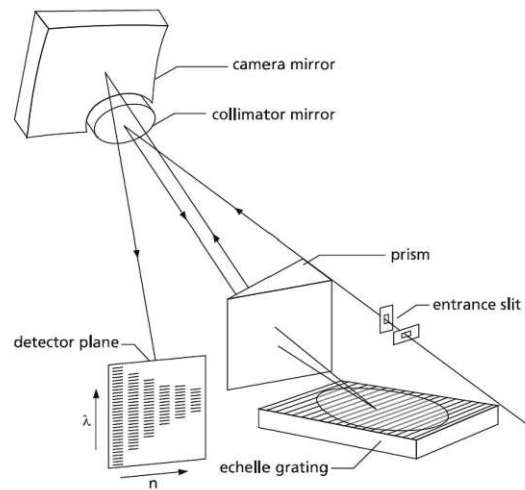


Figure 2.7: The arrangement of a typical echelle monochromator. Wavelength separation is performed by two dispersive elements: a prism and a grating. A two-dimensional plot of separated dispersing orders is schematically shown at the detector plane [33].

In combination with a suitable detection system, echelle monochromators allow the simultaneous coverage of a broad spectral width at a high resolving power. Echelle spectrographs consist of two dispersion components: a grating and a prism. The first dispersing element, either a prism or a grating, has the function of an "order sorter" (cross-dispersing element). The other dispersing element is placed perpendicularly at the first element. This has the purpose to generate an orthogonal shift between the single orders, so a two-dimensional plot of wavelengths and dispersion orders is achieved. In other words: the first element helps to avoid overlapping between different wavelengths at given diffraction orders. Echelle monochromators thus require appropriate detectors, allowing a projection of the focal plane of the dispersion on a bi-dimensional array of sensors. The read-out is carried out per each line of the array, converting rows of different diffraction orders into a linear spectrum. The great deal with echelle spectrographs comes with the high dispersion in all orders, and thereby showing a constant spectral resolution over the whole spectrum. Dispersive spectrographs with their low resolution presuppose the selection of one wavelength at their exit (at the slit). Echelle spectrographs however do

not require such an initial selection, which makes simultaneous detection and thus multi-elemental analysis easier. This provides a pleasant advantage against previously discussed wavelength selectors [34].

2.4 Detection Components

To convert an optical signal into an electrical signal, special electronic devices are needed. This step is necessary to generate a signal, that can further be treated by a data processing system of a computer. There is a broad range of known detectors. Two groups of detectors applied in LIBS experiments can be identified:

- time-resolved detectors
- light-integrating devices

The first type of detector recognizes incident light intensity within a defined time interval. Prominent examples of this type of detector are Photomultiplier Tubes (PMTs) and Photodiode Arrays (PDAs). PMTs consist of a vacuum tube and multiple dynodes. The signal in PMTs is generated by a photosensitive material (a cathode), generating a signal which is in direct proportion to the amount of light hitting on it. Electrons are ejected by impinging photons. Following, the ejected electrons are accelerated onto a positive poled second dynode. This marks a repetitious process and we observe a cascade of electron ejections, resulting in a measurable photocurrent, which is tapped and amplified. The whole process is based on the photoelectric effect. A schematic drawing of a PMT is shown in [Figure 2.8](#).

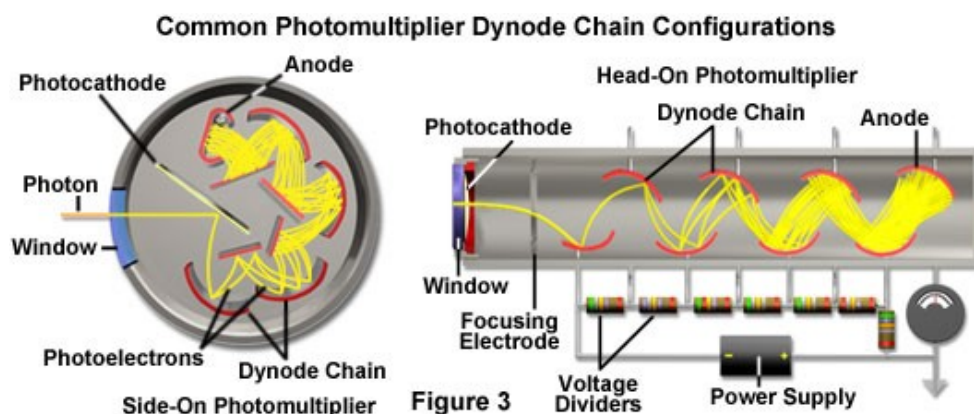


Figure 2.8: A side-on PMT (left) and a head-on PMT (right). The electron cascade is drawn yellow [53].

The drawback of PMTs becomes obvious since the detection of one single emission line requires a single PMT. As a result, the number of simultaneously detectable lines is limited drastically- which means it is not possible to record a full spectrum or a broad spectral range. Nonetheless, PMTs show excellent detectivity in the visible spectral region. Therefore, applications in very specific scientific problems are described, where high sensitivity and high selectivity for single emission lines are required.

To solve the problem of simultaneous detection, PDAs are often used in LIBS experiments as detectors. As the name suggests, PDAs consist of a linear array of up to thousands of single diodes. The discrete diodes are mounted on an integrated circuit, consisting of common n-type silicon. If a photon impinges on a diode, an electron is ejected and leaves an electron hole behind. Released electrons move to the nearest PIN junction and a charge difference is observed. The charge at each position on the array is read out after discrete time intervals, the so-called integration time. The dispersed spectral components are projected onto the diode array. The read-out at specific positions allows detecting single spectral features. Conventional PDAs consist of up to 4096 single diodes. A single diode has a diameter of about 10-25 μm [34][48].

An advancement of conventional PDAs are Charge-Coupled Devices (CCDs). Unlike PDAs, CCDs do not consist of a separate circuit. The whole detector consists of an array of photosensitive units at a microscopic scale (Pixels), which are produced on a silicon substrate by etching technologies. Again, this constitutes a bi-dimensional array, which makes the recording of the impinging radiation feasible. Photons, interacting with the silicon-oxide interface, eject electrons. A charge is generated which is stored in the semiconductor substrate below. The charge itself is directly proportional to the incoming light. The principle of CCDs is to apply a driving voltage at exactly defined time intervals. This evokes a charge shift from one pixel to the adjacent one within a column. This is called a vertical shift register. Another horizontal shift register is applied at the end of each row, transporting the charge content of each vertical column to the neighboring column at the same time. Both shift registers deliver a charge which is amplified into a processable voltage by an analogue-digital converter. On account of the bi-dimensional array and the charge scanning process, an image of the detected radiation can be constructed. Therein lies the great advantage of CCD detectors, making them ideal for combination with echelle monochromators. In combination, simultaneous detection of multiple wavelengths and also multiple spectra is possible, allowing straightforward multi-element analysis. A typical setup of a bi-dimensional CCD is shown in [Figure 2.9](#). CCDs are among the group of light-integrating devices.

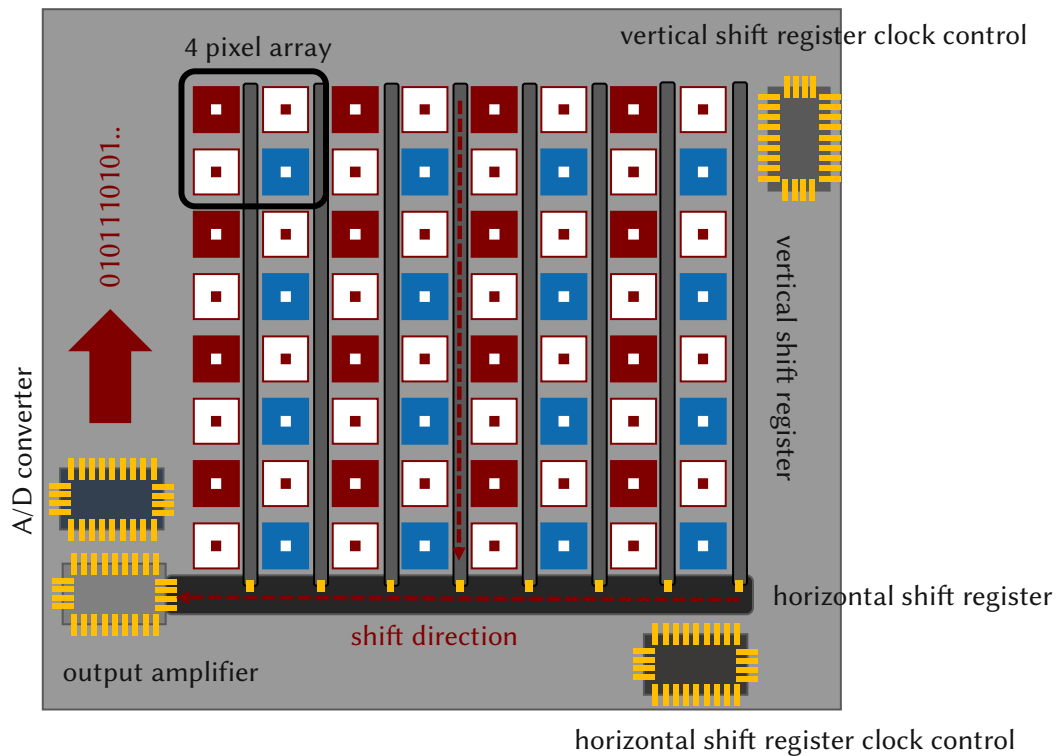


Figure 2.9: Setup of a CCD chip [54]. The precisely timed driving voltage pulse is applied by a register clock control.

At this point, it has to be mentioned, that although not described in detail in this section, also linear arrangements of PDAs and CCDs do exist. Such detectors are more often combined with customary spectrometers.

To enhance the sensitivity of CCD type detectors, Intensified Charge-Coupled Device (ICCD), further developed designs of the CCD were invented. ICCDs consist of a conventional CCD which is connected to a photocathode, a Microchannel Plate (MCP) and a phosphorous screen, working as an image intensifier. In this section, the working principle of PMTs was described in detail. A MCP is nothing more than a plate, containing many small channels, every single one working as a PMT. The channels are designed at a certain angle or curvature, thus preventing linear passing along a normal axis to the plate. If photons impinge on the pre-connected photocathode, again electrons are ejected and accelerated onto the MCP by an electric field. If hitting on a channel, incoming electrons eject secondary electrons

which are multiplied in a cascade process. In this way, an amplification of the signal is made. At the end of the channels, the electrons hit on an anodic poled phosphorous screen, where electrons are reconverted into photons which are directly guided onto the CCD. This requires an optical transmitter, such as focusing lenses or (more conventional) optical fibers. A scheme of a typical ICCD is shown in Figure 2.10.

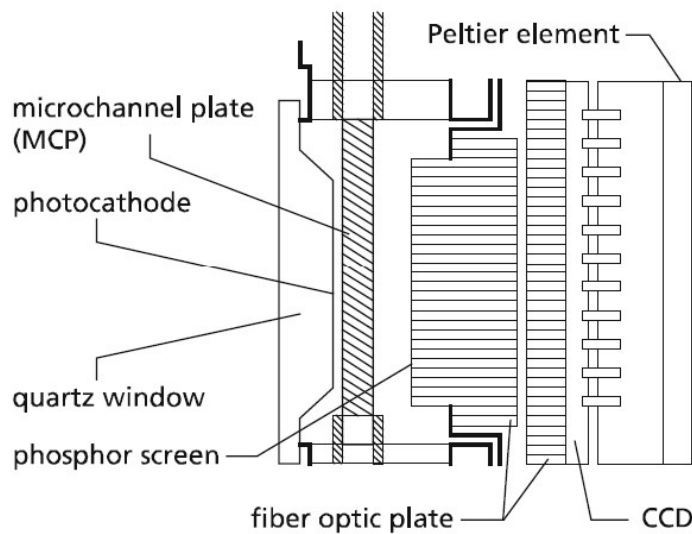


Figure 2.10: Schematic setup of a typical ICCD chip. Angled channels in the MCP can be seen. Heat development at the CCD during photon registration and signal processing is countered by a Peltier cooling-element [33].

By guiding the amplified photons directly onto the pixel domains, ICCDs reach an extremely high sensitivity. As a matter of fact, this marks such an efficient amplification process, that even a single photon can trigger the detection system. The amplification can be directly controlled by manipulating the voltage between the photocathode and the anodic phosphorous screen. Even more, the image intensifier can be used as a shutter, by simply reversing the polarity of the voltage. Then, passing photons become rapidly decelerated and finally accelerated in the opposite direction, leaving at the entrance side of the MCP. The absence of passing electrons, hitting on the phosphorous screen, leads to immediate termination of the photon

generation. This describes the so-called gating process, which allows defining a discrete time range. Configuration of a very defined integration interval is, therefore, possible, which is necessary to obtain signals resulting from certain transitions in e.g. molecular systems. Optimized time gating offers a way to improve S/N ratios in collected spectra by choosing the gate width as instrument parameter.

2.5 Molecular LIBS of AIO

The detection of AIO comes with major benefits. Firstly, AIO represents a species showing intense molecular emission, ranging from the ultraviolet to the orange part of the spectrum. As mentioned before, a characteristic band structure can be observed for the blue-green spectrum between 464 and 520 nm. We observe a structure, that seems to be divided into six subsystems between 445 and 545 nm. Three major band progressions show a band, ranging from 464 nm to 480 nm, a band ranging from 484 nm to 500 nm and finally a band ranging from 510 nm to 520 nm, resulting from pumping the resonant $X^2\Sigma^+ - B^2\Sigma^+(1,0)$ and $(0,0)$ states [55]. Single peaks at 508 nm, 510, 512 and 516 nm are a result of collision processes in the plasma. The whole system is shown in **Figure 2.11**.

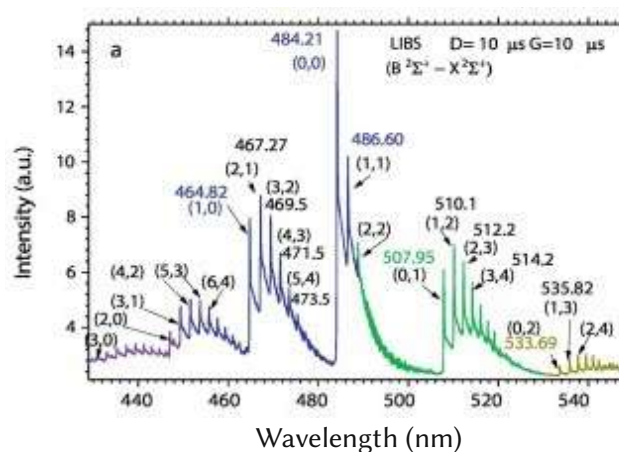


Figure 2.11: The Al^6O blue-green system. The five subsystems are clearly visible [55].

Notably, the last subsystem is of interest, due to few spectral interferences by environmentally abundant elements showing (molecular) emissions on the same spectral range. Such elements are for instance iron (Fe), copper (Cu), magnesium (Mg), scandium (Sc), lanthanum (La), yttrium (Y) etc. Especially, the formation of oxides becomes an issue if operating in this spectral range. To separate molecular emission from atomic lines, gate delay and gate width are adapted. This states a procedure, which depends on the chosen setup and has to be carried out for each sample and each apparatus. Typical gate delays and gate widths are of the order of some up to some tens of microseconds.

Bol'shakov et al. showed the feasibility of Laser Ablation Molecular Isotopic Spectroscopy (LAMIS) on this system. In Figure 2.12 the isotopic shift between Al^{16}O and Al^{18}O is shown [37].

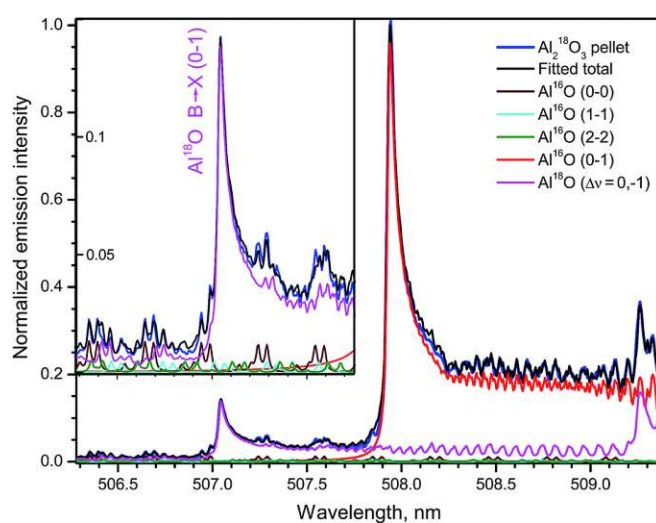


Figure 2.12: LIBS spectrum of the peak at 507 nm. The spectra were acquired with 20 μs gate delay. 100 spectra were accumulated [37].

At 507.93 nm the band head (0,1) of Al^{16}O can be seen clearly, while the band head of Al^{18}O lies at 507,04 nm, showing an isotopic shift of about one nanometer. The spectrum was recorded during ablation of an ^{18}O enriched Al_2O_3 pellet, averaged over 100 single-shot spectra. The amount of ^{18}O was about 10%, which is represented

by the ratio between the two band heights. Through this example, we see that an isotopic shift in this part of the band system can be detected using a common single-pulse LIBS setup.

3 Experimental

3.1 LIBS Spectrometer and Experimental Setup

The experimental setup for LIBS measurements conducted in this work consisted of a 266 nm Nd:YAG laser (Quantel, Bozeman, MT, USA) and a J200 Tandem LIBS instrument of Applied Spectra (Berkeley, CA, USA). Additionally, an external spectrometer was connected via optical fibers. For the evaporation experiments, an Electrothermal Vaporization (ETV) instrument (ETV 4000 of Spectral Systems, Fürstfeldbruck, Germany) was utilized. The whole setup is shown in [Figure 3.1](#).

The laser was a Q-switched Nd:YAG laser with an operating wavelength of 266 nm, reached by fourfold frequency multiplication, with a pulsing frequency of 10 Hz and a pulse duration of 6 ns. Determination of the laser energy was frequently carried out by an internally installed power meter and showed an actual laser power between 1 and 6 mJ. The laser optics inside the J200 Tandem allowed focusing of the laser beam between 60 and 200 μm .

The J200 Tandem is a LIBS instrument containing a focusing optics and a spectrometer containing a six channel CCD-based broadband spectrometer using a Czerny-Turner setup, covering a wavelength range from 187 to 1047 nm. A movable stage was implemented, allowing precise control of ablation patterns and positioning. With an installed microscope camera optics, the setting of ablation patterns and the tracking of the ablation process was possible. A gas-tight ablation chamber was mounted on

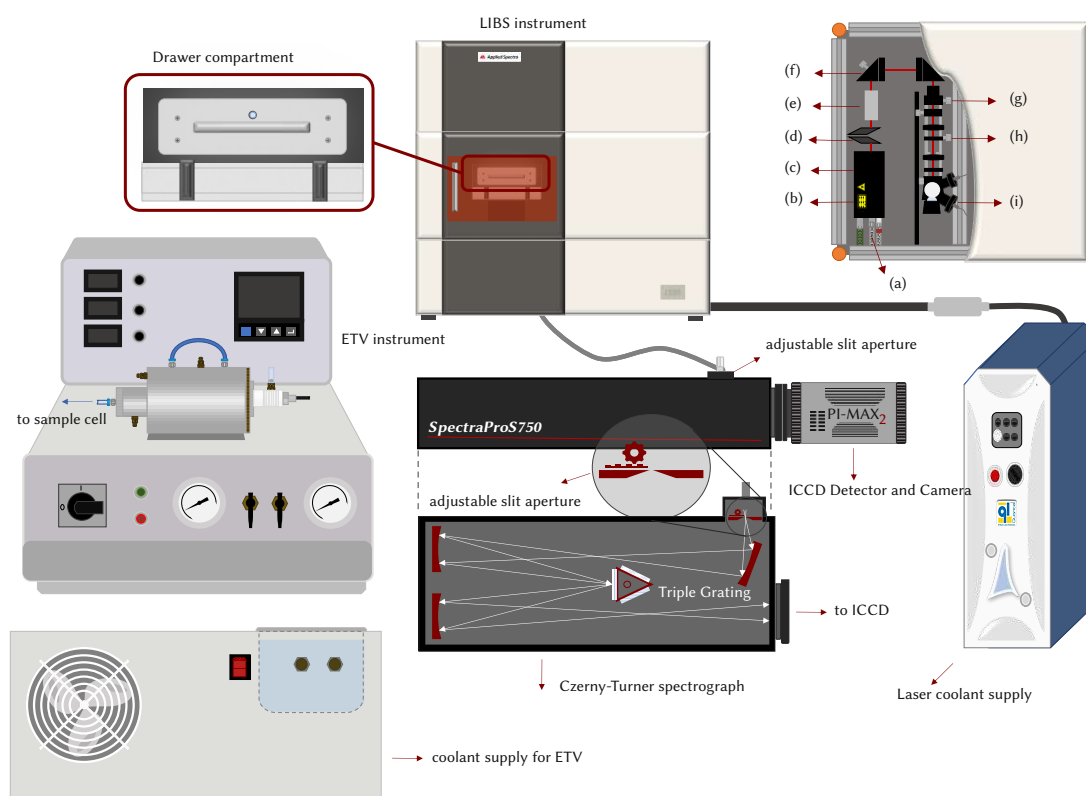


Figure 3.1: The chosen LIBS setup consisting of a LIBS instrument, an external spectrometer and an ETV apparatus. Top right: the beam path inside the LIBS instrument (top view) is shown. (a) power and coolant supply (b) laser (c) harmonics (d) dichroics (e) attenuator (f) adjustable mirror (h) aperture (i) collection optics.

the stage, allowing to flush the environment with inert gases. This ablation chamber was built as a drawer compartment allowing to change samples rapidly and uncomplicated (see Figure 3.2). Solid samples were placed in a Teflon inlet, fitting perfectly into the tray. The system software Axiom 2.0 enabled controlling of parameters for each measurement, and the device settings, also including the determination of a gate delay, the laser energy etc. Data collection and treatment was performed with Aurora v18., an included software delivered by Applied Spectra Inc.

As an external spectrometer, an Acton S750 Monochromator by Princeton Instruments (Teledyne Princeton Instruments, NJ, USA) with a Czerny-Turner design was installed. This spectrometer contained three different gratings, with 300, 1200 and 2400 grooves per mm. The spectrometer was connected to a PI-MAX2 High Speed

ICCD camera.

The data acquisition was performed using WinSpec, a corporate software by Princeton Instruments, also allowing advanced settings of the gate delay, gate width, the number of accumulated spectra and various other parameters, controlling the ICCD detector. The external spectrometer was coupled to the J200 Tandem via optical fibers. The fiber was attached to the spectrometer by a screw connection. An entrance slit allowed to regulate the amount of incoming light and to create a narrower beam and thus enhancing the spectral resolution. The slit width could be manipulated up to 2 μm .

3.2 Setup for Evaporation of H_2^{18}O

For aerosols and gaseous components, a different inlet was chosen (see [Figure 3.2](#)). A suitable aluminum holder was placed into the tray, allowing the positioning of a cell in the center of the tray. The cell itself consisted of an aluminum cylinder, with a cylindrical bore. At the top side, the cell was sealed by a bolt connection with a cover, containing a quartz window. The quartz window showed nearly complete transmissivity for the 266 nm laser beam, allowing laser ablation inside the cell. To transport gaseous components into the cell, two paired entrances were installed, already containing a DIN ISO 4762 M6 thread, enabling connection with suitable tube fittings. By this means, Teflon tubes were connected to the cell, creating a transport line to the ETV.

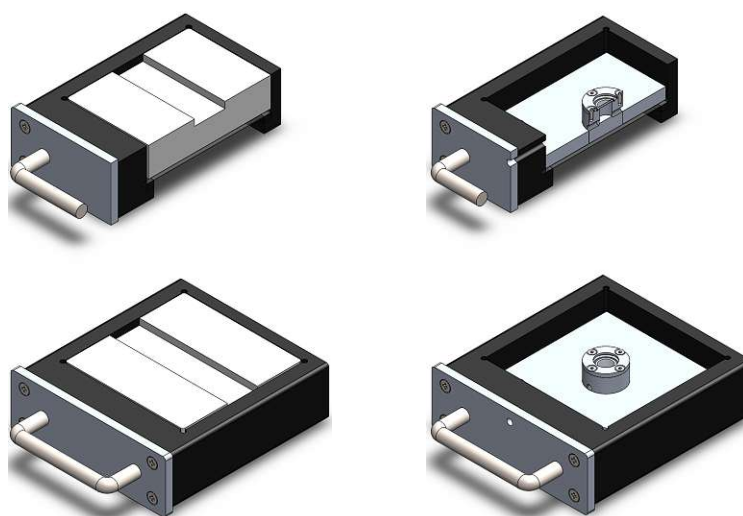


Figure 3.2: The drawer, containing a Teflon inlet. Solid samples are placed in the recess of the inlet (left). A holder made from aluminum and the sample cell used for measurements applying the ETV instrument, containing a cover, a screw bolt connection, a quartz window, a viton seal (right).

A schematic illustration of the inside of the ETV is pictured in [Figure 3.3](#). Liquid samples were placed in a graphite boat, which was placed directly into a graphite tube. The tube itself was permanently installed in a graphite furnace, which also worked as an electrical contact. The Instrument contained a digital surface, allowing to specify a temperature program. The liquid sample thus was heated rapidly within a customer pre-set time interval, the vapor was carried out by an applied argon flow (carrier flow) and transported to the cell inside the chamber by Teflon tubes. Additionally, an argon bypass flow was applied, to optimize the transport and minimize condensation effects inside the ETV.

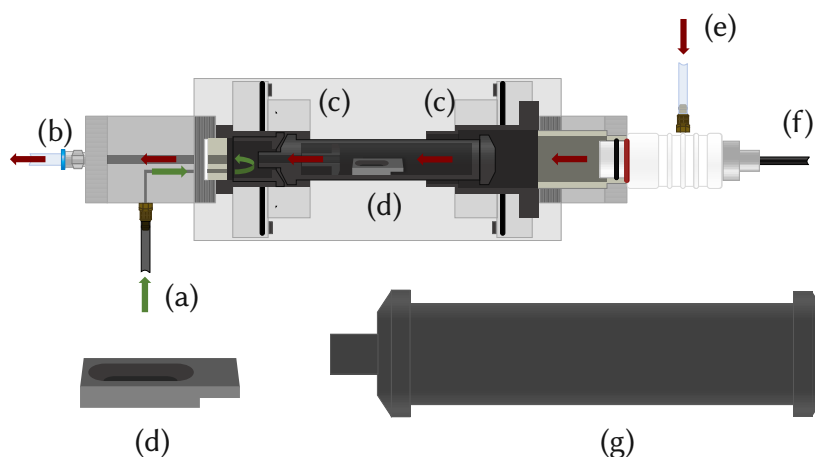


Figure 3.3: Inside of the ETV. (a) bypass argon flow, (b) Teflon tube connected to the sample cell (see Figure 3.2), (c) cooled brackets, (d) graphite boat, (e) carrier argon flow, (f) connection cable to a thermoelement for temperature control, (g) graphite furnace.

3.3 Materials and Sample Preparation

Two sets of pellets with different amounts of aluminum and oxygen were produced. For this purpose, Al_2O_3 (Alfa Aesar® γ -phase, 99.98% 0.01-0.02 μm powder) and AlN (Sigma Aldrich, nanopowder, <100 nm nanopowder) or aluminum powder (Fluka, >99% purum, 100-200 micron powder) were homogenized in a mortar and mixed on a Vortex device. The pellets were finally formed by cold isostatic pressing for 30 seconds at 15 bar. This way, pellets with molar ratios of Al:O between 10:1 and 1:1.5 were produced. A detailed description of mass weights is attached in the [Appendix \(Table .1, Table .2\)](#).

For the measurements containing H_2^{18}O , water, enriched with ^{18}O (>98%, Campro scientific) was added to deionized water. Different calibration standards were created for the respective experiments. Detailed mass weights are shown in table (x) and (y) in the appendix below. Two sets of calibration standards were produced, one with 0, 10, 20, 30, 40, 50, 60, 70, 80, 90 and 100 %wt and one with 0, 25, 50, 75 and 100 %wt of H_2^{18}O ; diluted in H_2^{16}O . For the measurements containing evaporation using the ETV dilution steps of 0, 5, 10, 20 %wt H_2^{18}O in H_2^{16}O were produced. The

amounts of H_2^{18}O were also diluted in Acetonitrile (MeCN). The aluminum plate used in the evaporation experiments was an aluminum band, delivered by Merck (Aluminiumband, zur Analyse, p.a.).

3.4 Premeasurements

In an initial evaluation, experiments were made, to determine the measurability of the AIO system with the shown setup. For this purpose, at first, pellets with different molar amounts of Aluminum and oxygen were produced. The pellets were analyzed employing the CCD as well as the ICCD detector system. [Table 3.1](#) summarizes the initial operation parameters for LIBS measurements. Gate delay and gate width were optimized for these experiments.

Table 3.1: Initial LIBS parameters for premeasurements concerning pellets

Detector	Gate Delay	Gate Width	Laser Energy	Repetition Rate	Atmosphere	Shots	Spot Size
	(μs)	(μs)	(mJ)	(Hz)		()	(μm)
CCD	0.7	-	1.5	10	Ar	500	120
ICCD	5	10	1.5	10	Ar	200	120

Spectral Analysis focused on the spectral region between 507 and 515 nm. A different number of spectra was acquired and accumulated for the CCD (which required a far higher number of accumulated single shot spectra and (warmup-) shots) and the ICCD detector. The shots were spread over a 5×5 mm pattern which was placed directly at the pellet surface. Adjustments in the speed of the sample stage movement allowed to change the number of shots within a defined pattern. Different pattern structures are shown in [Figure 3.4](#). A narrow spot diameter was chosen, to obtain high irradiance. In this setup the use of the mentioned sample cell was

renounced, the sample pellets were placed directly on the Teflon insert inside the tray.

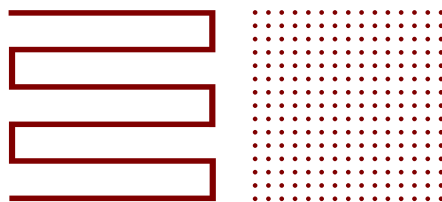


Figure 3.4: A meander pattern (left) and a point pattern (right).

Data acquisition took place in Axiom and WinSpec. For the ICCD detector the amplifying factor (gain) was set to 100, the slit was adjusted to $0.25\ \mu\text{m}$. To remove oxygen from ambient air, the chamber was flushed with argon ($2\ \text{L min}^{-1}$) for at least 20 minutes.

3.5 Premeasurements on the Evaporation of Water

In a further approach, water was introduced directly into the chamber, to test if the introduction of oxygen in the form of water into the plasma plume is possible. Special attention was set onto the retention time of introduced amounts of oxygen in the chamber, examining potential enrichment effects. In these experiments the sample cell was used and attached to a tube, guided through a heated sample vial filled with demineralized water and sealed with a septum. A gas flow of $1000\ \text{mL}$ argon per minute was applied and enriched with water vapor (see Figure 3.5). As substrate a small aluminum plate was placed into the sample cell, 200 shots were placed at the surface in a meander pattern. Initial LIBS parameters are presented in Table 3.2. Again, the chamber was flushed for 20 minutes. Data acquisition was performed at the ICCD system, the gain parameter was set to 100, the slit was set to $0.25\ \mu\text{m}$.

A variation of the last-mentioned experiment was carried out with isotope en-

riched water (H_2^{18}O). A small volume ($4\ \mu\text{L}$) was placed directly on the aluminum plate (placed at the Teflon insert), in flow direction of the argon flow, to enrich the atmosphere with vapor. A small Teflon ring was placed around the droplet, to prevent too quick and ensure homogeneous evaporation of the water drop. Consecutively, volumes with different molar amounts of isotope labeled water were introduced into the chamber, the same way. Linear calibration was made by a Partial Least Squares (PLS) method in Epina ImageLab. Chosen experimental parameters are presented in Table 3.2. A scheme of the arrangement is delivered in Figure 3.6.

Table 3.2: Parameters of the premeasurements containing evaporation of water.

Detector	Gate Delay	Gate Width	Laser Energy	Repetition Rate	Atmosphere	Shots	Spot Size
	(μs)	(μs)	(mJ)	(Hz)		()	(μm)
ICCD	1	10	1.5	10	Ar	200	120

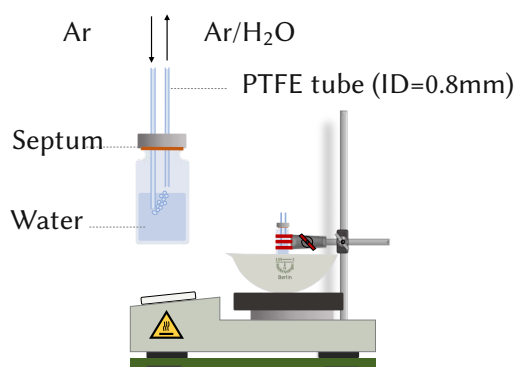


Figure 3.5: Arrangement used for water enrichment of an argon flow.

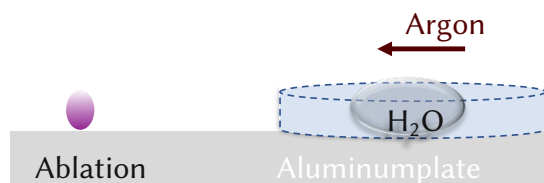


Figure 3.6: Schematic view of the H_2^{18}O droplet on the aluminum surface, protected by a Teflon ring.

3.6 Evaporation Measurements using ETV

To reach a rapid evaporation of small volumes of water, the ETV was directly connected with the sample cell inside the LIBS ablation chamber, containing again a small metallic aluminum plate. The graphite boat was for each measurement loaded with 10 μL of mixtures of water with different molar amounts of isotope labeled water. According to an optimized program, a temperature ramp was adjusted, starting at room temperature and reaching a maximum temperature of 150°C after 40 seconds. Maximum temperature was held constantly for 20 seconds before cooling down, leading to a complete evaporation of the sample. The applied program is shown in Figure 3.7.

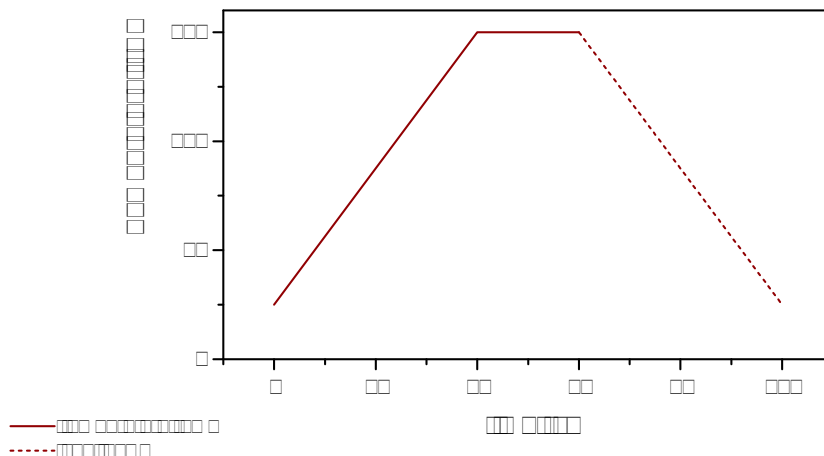


Figure 3.7: The temperature program for measurements containing evaporation of water by means of the ETV. Within 40 seconds a temperature of 150°C was reached, which was held constantly for 20 seconds before cooling down to room temperature again.

As the evaporation marks a continuous process, the amount of water reaching the sample chamber can not be assumed as a narrow peak-shaped profile. Likely, complete evaporation takes place over a certain time, leading to a broadening of the peak. Even worse, the vapor phase suffers broadening effects during the transport in an argon flow. This leads to a wider peak shape, covering a time interval of a few

seconds. To transfer the highest possible amount of water into the plasma, a high number of 1000 shots was chosen. Detection was performed at the ICCD detector, applying a slit of 0.25 μm , choosing the medium resolution grating (1200 g/mm). The chamber was flushed with argon for at least 20 minutes. The initial parameters of this series of measurements are shown in Table 3.3.

Table 3.3: Parameters of the premeasurements containing evaporation of water using the ETV

Detector	Gate Delay	Gate Width	Laser Energy	Repetition Rate	Atmosphere	Shots	Spot Size
	(μs)	(μs)	(mJ)	(Hz)		()	(μm)
ICCD	1	10	1.5	10	Ar	500-1000	120

4 Results and Discussion

4.1 Initial Measurements and Determination of Measurement Parameters

Initial experiments also provided the opportunity to gain routine in the measurement process. A procedure was introduced, which was applied for every following measurement to reduce fluctuations in the working process. The goal in this step was to generate reproducible data and to find optimized parameter settings. At first, a simple measurement was carried out on metallic aluminum to examine the measurability of the AlO molecular emission by the present setup. This measurement was carried out at ambient air, serving as a source of oxygen, therefore Al¹⁶O was measured. In the beginning, suitable gate delays were determined for the CCD detection system. Then determination of the laser energy and number of shots was carried out on a pure Al₂O₃ pellet.

In an initial approach, a gate delay of 0.7 μs, the highest possible energy of 80% (about 1.5 mJ at the time of measurement), and a high number of 500 shots was chosen (see Table 3.1). Those initial parameters were optimized during the following experiments. In Figure 4.1 we see an evolution of collected spectra according to Figure 2.2. A spectrum collected at a gate delay of 0.1 μs shows the expected band system in the examined spectral region (cf. Figure 2.12). Single peaks are mostly superimposed by a continuous background at this gate delay, which was therefore

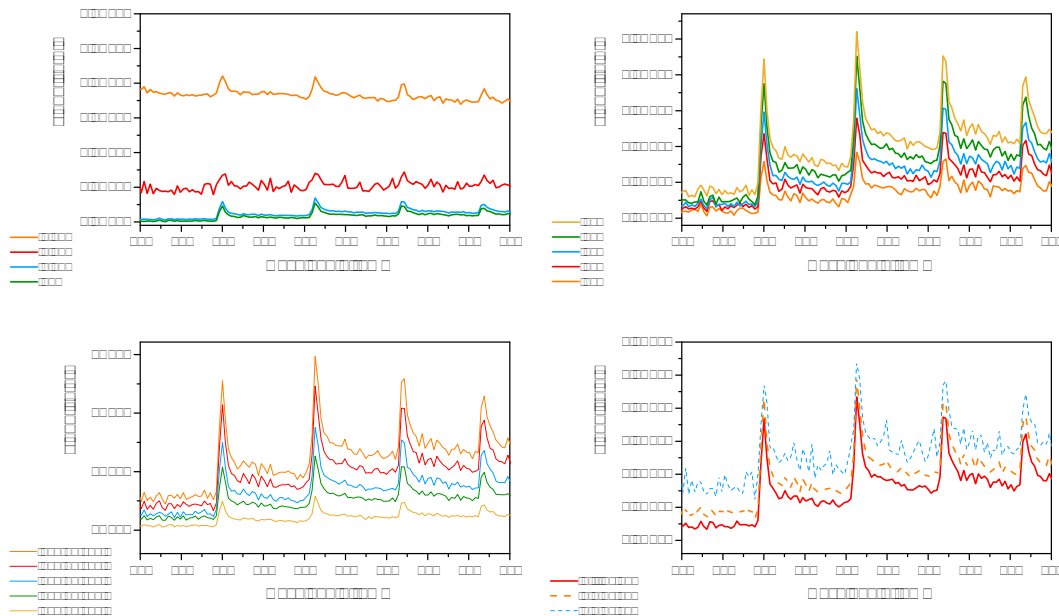


Figure 4.1: Finding of experiment parameters at the CCD detector. Initial values can be found in Table 3.1. Top left: adjustment of gate delays. Top right: influence of the laser energy on the signal intensity. Below left: influence of the different amounts of shots. Below right: optimized signal collection. A gate delay of $1 \mu\text{s}$, a laser energy of 80% and a number of 200 shots were found as suitable parameters.

prolonged. With increasing gate delay, signals start to show a better S/N and single bands can be clearly identified. The largest gate delay presented in Figure 4.1 ($1 \mu\text{s}$), shows the best S/N, hence, this value was used in further experiments. The variation of the laser energy and the number of (warmup-)shots show a similar, already expected trend. Maximum laser energy and a higher number of accumulated shots result in higher intensities. A laser energy of about 1.1 mJ (80%) can be seen as sufficient to collect pronounced AIO band spectra with sufficient resolution. At the CCD detection system, the acquisition of 200 accumulated shots delivered two resolved bands, allowing to make a compromise between a fast, reliable measurement within this range. A number of 100 accumulated shots shows low resolution of bands and was determined to be insufficient for the chosen experiments. Optimized parameters are shown in Figure 4.1 and provided a starting point for the finding of parameters for measurements applying the ICCD detector.

It can also be shown that the oxygen present in the formed AlO molecules, causing the molecular emission, derives from the ambient air in the chamber. After flushing the chamber with argon for at least 20 minutes, recorded spectra do not show distinguishable AlO Bands in the region between 506 and 515 nm anymore. This behavior is shown in Figure 4.2. Thus, it can be excluded that recorded emission bands are a result of undissociated fragments of AlO being excited by the laser.

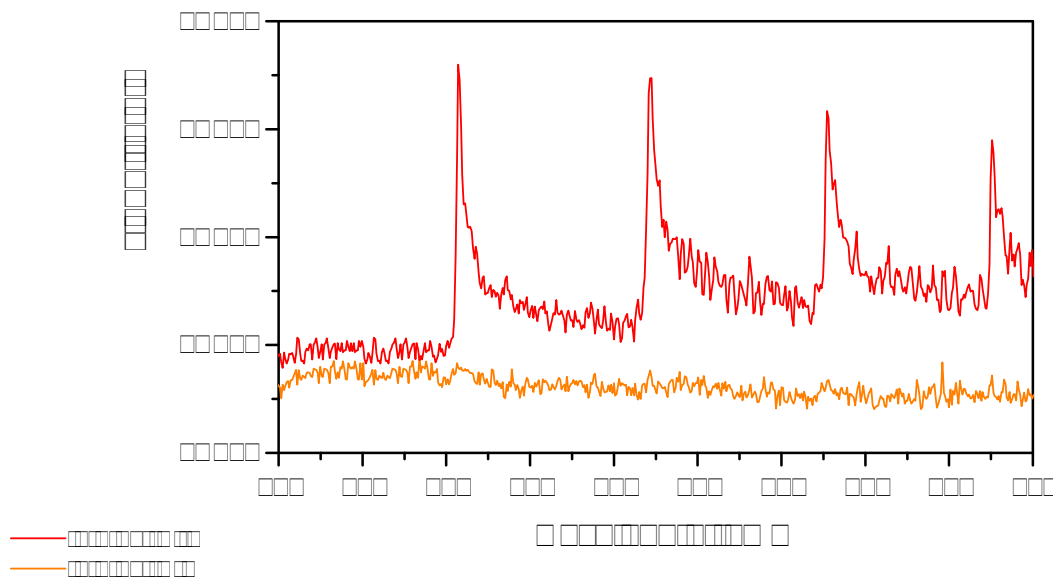


Figure 4.2: Recorded spectra under ambient air (red) and argon atmosphere (orange). A small gate delay of $0.2 \mu\text{s}$ was chosen, to detect even small amounts of formed AlO. Detection was made at the ICCD detector, to take full advantage of the better sensitivity. The gain was set to 100, a gate width of $10 \mu\text{s}$ was chosen. A small spotsize of $100 \mu\text{m}$ was set to ensure high irradiance. Under argon atmosphere Peaks at 507, 510, 512 and 514 nm disappear, hinting the absence of AlO formation in the plasma.

The results of those experiments show good measurability of the expected signals in the spectral range of interest with the chosen setup. The measurement of reported AlO signals was therefore possible. Sufficient signal resolution was observed, allowing to distinguish bands associated with Al^{16}O and Al^{18}O , showing an isotopic shift of about one nanometer. Detection of a pronounced isotopic shift is necessary for differentiation of the isotopic AlO bands. Further, adequate inertness of the chamber was determined, purging with argon for at least 20 minutes can be assessed as

satisfactory to guarantee undisturbed work by ambient air.

4.2 Premeasurements

Parameters settings from [section 4.1](#) were transferred to the measurements of the $\text{Al}_2\text{O}_3/\text{Al}$ pellets with varying composition. Expected molecular emission was also observed for pellet samples, demonstrating that observations reported in literature can also be made accessible with the applied setup (cf. [section 2.5](#)). Experiments were performed under argon atmosphere, thus the oxygen present in the pellet was the only source of oxygen for AlO formation. Again, gate delays were analyzed in an initial experiment, reaching from 0.1 to 1 μs . In these measurements, 500 shots were accumulated. For optimization of experiment parameters, again a pure Al_2O_3 pellet was utilized.

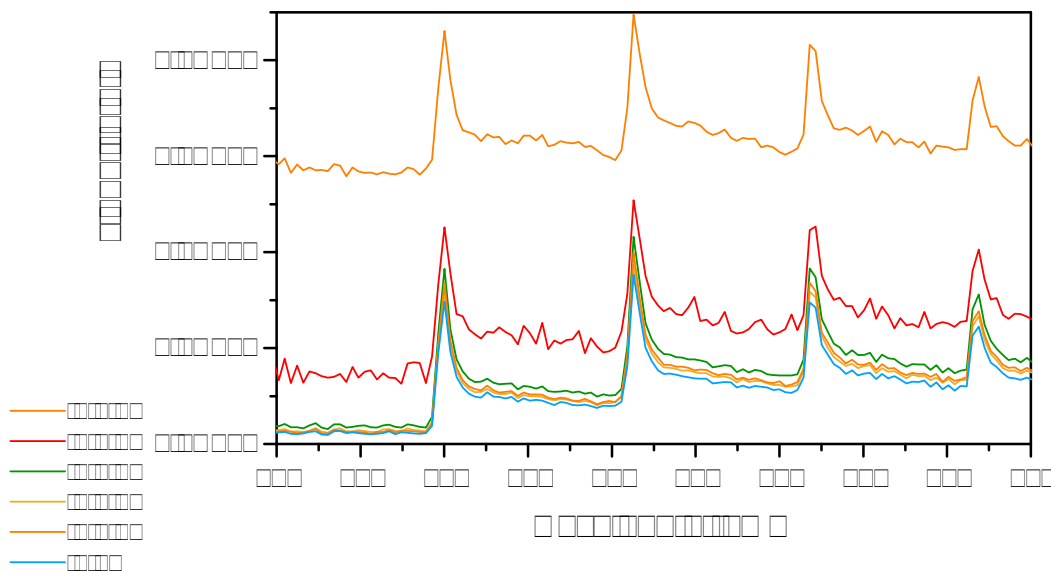


Figure 4.3: Fine adjustment of gate delay at an Al_2O_3 pellet, showing a decrease in absolute signal intensity at larger gate delays.

Figure 4.3 shows a detailed fine adjustment and optimization of experiment parameters for the $\text{Al}_2\text{O}_3/\text{Al}$ pellets. A rapid decrease in absolute signal intensity can be recognized as time proceeds, leading to very similar well resolved spectra in a time range between $0.5 \mu\text{s}$ and $1 \mu\text{s}$. This marks the time regime where the optimal S/Ns can be acquired, while still maintaining sufficient signal intensities. The absolute loss in signal intensity for larger gate delays was rated as too high, delivering weakly pronounced peaks.

Until now experiments were initially conducted under argon atmosphere. Consideration was given whether helium is a suitable plasma gas. This was examined at the ICCD detector, on an ordinary Al_2O_3 pellet. Following, the ablation chamber was flushed with either argon or helium at different flow rates (500 and 1000 mL min^{-1}) for at least 20 minutes. After this purging procedure, 200 spectra were recorded and accumulated. A gate delay of $0.7 \mu\text{s}$ was chosen since this measurement was conducted during the optimization of gate delays on the Al_2O_3 pellet, and optimized delay parameters were not finally set. However, an adequate signal was recorded, to estimate possible effects of different atmospheres. The results are shown in Figure 4.4.

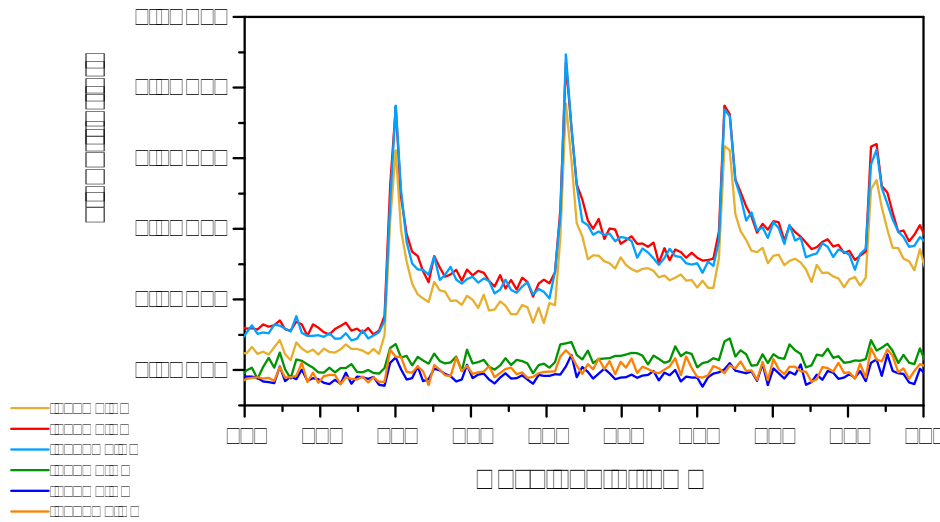


Figure 4.4: Development of AlO molecular emission under different atmospheres. Helium clearly suppresses signal development of discussed AlO emission bands. 200 shots were acquired at a gate delay of $1 \mu\text{s}$ and a gate width of $10 \mu\text{s}$.

It can be recognized, that regardless of the chosen flow rate, helium discriminates the production of the characteristic AlO bands in the known region. In the following experiments, helium, therefore, was not used as atmosphere gas in the cell, the chamber, or as flow gas in the transfer line.

With optimized experiment parameters, attention was given to a possible dependence of observed signal intensities, on oxygen amounts in the sample, for this would allow direct quantification of the recorded signals.

To examine this, a set of pellets of Al_2O_3 and Al powder was produced, varying the molar amounts of aluminum and oxygen by addition of aluminum powder. In **Figure 4.5** results for pellets with stoichiometric Al:O ratios of 1:1, 2:1 and 5:1 are shown. The pellet with equimolar amounts of aluminum and oxygen (1:1) seems to produce the highest observable AlO signal. Pellets with enhanced molar amounts of aluminum show lower signals, indicating a proportional relationship between oxygen content and signal intensity of the AlO emission bands.

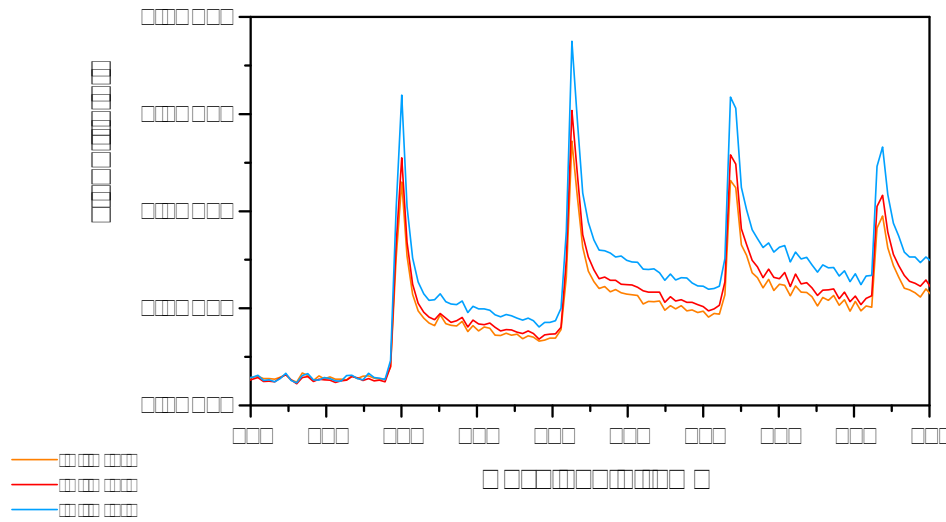


Figure 4.5: Different signal intensities in recorded spectra of the set of $\text{Al}_2\text{O}_3/\text{Al}$ pellets, showing an increasing trend as the amount of oxygen in the sample increases. Measurement took place at a gate delay of $0.7 \mu\text{s}$ at the CCD detector. 500 shots were acquired in both spectra.

Although these first experiments with pressed pellets delivered promising results, severe problems concerning the homogeneity of the prepared samples were observed which demanded further improvements. Besides, it could not be excluded, that observed progression in signal intensity for higher oxygen amounts was only an effect caused by better sample ablation. The different particle sizes and the different chemical properties of Al_2O_3 and metallic aluminum particles, used for sample preparation, could cause such effects. To further examine a possible connection between signal intensity and oxygen amounts, a second set of pellets, containing Al_2O_3 and AlN was produced, showing better homogenization than the $\text{Al}_2\text{O}_3/\text{Al}$ mixture and providing a system, containing no metallic aluminum. The idea was to eliminate possible differences in the ablation process by introducing an aluminum compound showing similar properties to Al_2O_3 . A further benefit of AlN was the lack of an Al_2O_3 layer as likewise at the surface of metallic aluminum particles.

This is especially useful when preparing pellets with different stoichiometric amounts of oxygen. At first, experiment parameters were again reviewed at the CCD system,

before applying the ICCD detector. This might appear superfluous but represents a necessary process, to avoid any damage from the more sensitive ICCD detector. The previously discussed, apparent effect outlined in Figure 4.5 was observed again. Sample pellets with higher amounts of oxygen produced higher signals. Recorded spectra are presented in Figure 4.6.

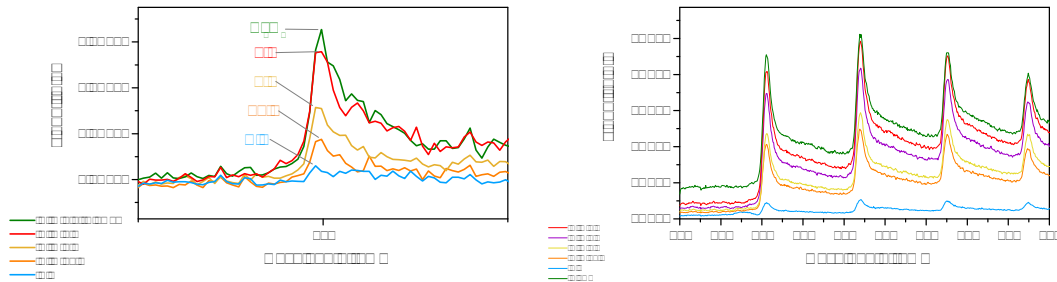


Figure 4.6: Different signal intensities of one single band (left) and the whole band system (right) at different oxygen contents in the $\text{Al}_2\text{O}_3/\text{AlN}$ pellets. 200 shots were accumulated at a gate delay of $1 \mu\text{s}$ and a gate width of $10 \mu\text{s}$. Detection was performed at the ICCD detector.

Spectra recorded at a gate delay of $1 \mu\text{s}$ (gate width $10 \mu\text{s}$) were chosen for data evaluation. 200 shots were acquired and accumulated at the ICCD detector. To provide a better overview of the noticed trend, relative peak heights were read out at the peak maximum at 508, 510 and 512 nm and plotted against molar fractions of oxygen. In a further step single peak areas were integrated. For this, a linear baseline correction was performed, and the resulting peak areas were summed. Both curves show a similar trend (see Figure 4.7).

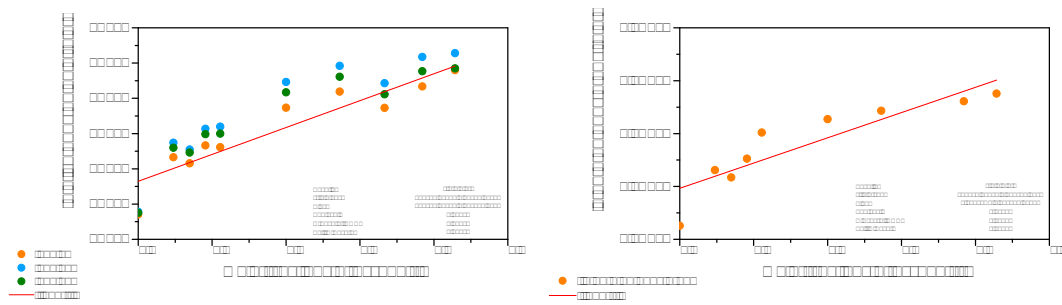


Figure 4.7: Read out peak heights (left) and integrated peak areas (right) plotted against molar fractions of oxygen in the sample pellets. An increase in signal intensity with increasing oxygen amount can be observed.

Signal values at molar fractions at 0.11 and 0.33, representing Al:O ratios of 4:1 and 1:1 can be identified as outliers, potentially due to errors in the production or measurement of the pellets, and were therefore not considered in the peak integration process. The increase of the signal intensities at increasing oxygen amounts in the sample material can thus be assigned to a linear increasing behavior. This result was an important indicator, showing the possibility to receive different signal intensities at different molar amounts of AlO in the Laser Induced Plasma (LIP) and thus opening a way to create a calibration.

4.3 Premeasurements on the Evaporation of Water

4.3.1 Premeasurements on the Evaporation of H_2^{16}O

In the measurements performed on pellets of varying composition, oxygen was already part of the investigated samples. To examine, whether the recorded AlO emission derives from undissociated, excited fragments, originating from the samples or results from AlO formation of fully dissociated atoms during recombination processes in the plasma afterglow a further approach was chosen. The idea was to introduce oxygen in the form of water to the plasma plume. This should ensure, that

oxygen, bound in formed AlO molecules, does not stem from the sample and make external introduction of oxygen to the plasma plume feasible. Following the setup shown in Figure 3.5, an argon flow was saturated with H₂O and guided directly into the plasma. The measurements were conducted at the ICCD detector, a gate delay of 1 μs was chosen, 200 spectra were accumulated. The results of the introduction of a water loaded argon flow direct into the plasma are shown in Figure 4.8.

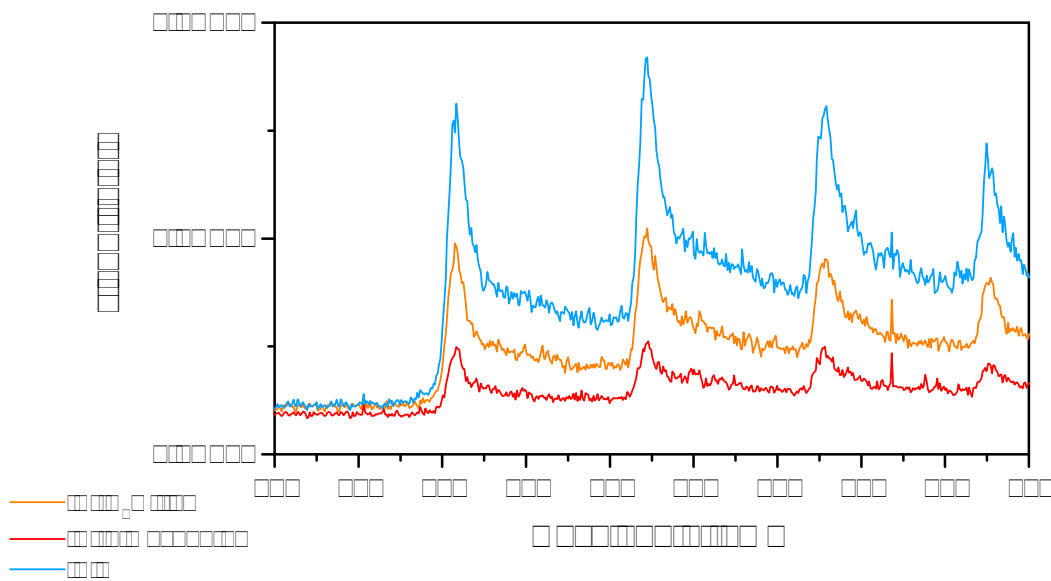


Figure 4.8: Development of the AlO band at 507 nm under dry argon atmosphere without saturation of water (red spectrum) and under the influence of an argon flow loaded with water (orange spectrum) and under ambient conditions (blue spectrum).

Spectra shown in Figure 4.8 demonstrate three different situations: Under ambient air, after flushing the chamber with argon (at least 20 minutes) and finally the measurement including the applied Ar/ H₂¹⁶O flow. It can be recognized, that even after flushing with argon, still AlO bands occur. This can be explained by residual humidity in the ablation chamber, introduced by previous experiments. Polar groups at the surface of aluminum absorb water to a relevant extent. Such polar groups consist of hydroxide groups, being formed at an omnipresent oxide layer at the outmost surface of metallic aluminum. Potentially, this leads to an absorption of

water, generating the observed signals, although no water or oxygen is introduced. In addition, the presence of residual oxygen from ambient air cannot be fully excluded. However, discussed bands are of noticeable lower intensities if compared to the recognizable bands, recorded under ambient air (blue spectrum). After applying the water-saturated argon flow, a distinctive signal development in the AIO bands is observed (orange spectrum) compared with spectra recorded under dry argon atmosphere (red spectrum).

Obviously, the saturation of an argon flow with water vapor is an opportunity to guide water, an oxygen-containing compound, directly into the plasma. This process is causing a visible difference in the signal intensities of observed signals. From this result, it was also concluded, that resulting AIO molecular emission does not result from undissociated fragments of already existing compounds of aluminum and oxygen. It is therefore possible to induce a reaction between aluminum and externally introduced oxygen in the plasma afterglow.

As already mentioned, the introduction of water to the cell by a water-loaded gas flow contains the risk of influencing further measurements, by enrichment of water in the cell. Water, and hence oxygen contents introduced in the following experiments, can be adulterated by this effect. However, it is possible to purge the cell by applying a dry gas flow. **Figure 4.9** shows that after stopping the water-loaded argon flow and applying a dry argon flow (2L min⁻¹) for at least 5 minutes to the cell, is satisfactory to reduce this effect. Purging steps of at least 15 minutes were subsequently carried out after each measurement, involving the evaporation of water. After such a purging treatment, recorded signals show similar intensities to signals collected before application of a water-loaded argon flow. The remaining AIO bands can be seen as a constant background, that could not be eliminated, even after longer purging periods.

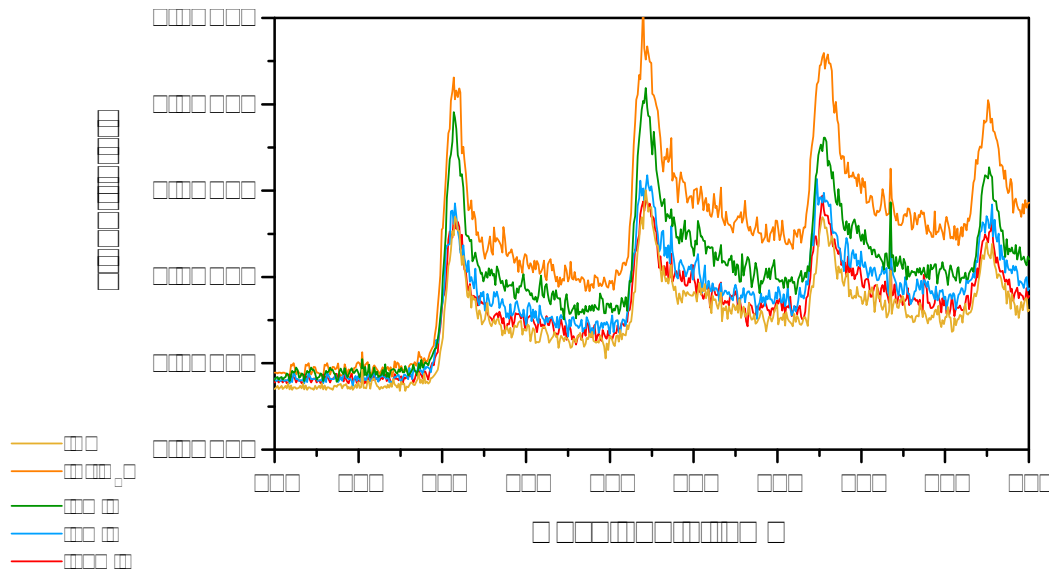


Figure 4.9: After flushing the chamber with argon (2L min⁻¹) for 5 minutes the influence of introduced vapor can no longer be recognized, leaving behind signals that provide a constant background. A gate delay of 1 μs was chosen, 150 shots were accumulated.

4.3.2 Premeasurements on the Evaporation of H₂¹⁸O

The results discussed in the last chapter above served as the basis for experiments containing H₂¹⁸O isotope enriched water as discussed in [section 3.5](#) (see [Figure 3.6](#)). It emerged, that a volume of 4 μL of isotope enriched water was sufficient to saturate the atmosphere in the chamber with vapor. The argon flow was optimized to 0.5 L per minute, reflecting a compromise between a flow rate high enough to reduce ambient air in the chamber to a tolerable minimum and a flow rate small enough to ensure a constant evaporation. A gate delay of 1 μs and a gate width of 10 μs was chosen. Again 200 shots were accumulated. Measurements were carried out at the ICCD detector. The meander pattern at the aluminum plate was placed at the largest possible distance to the droplet inside the Teflon insert. Overall, the spread was about 8 cm, to make sure, that the oxygen exclusively originated from the vapor phase in the argon flow stream overflowing the aluminum plate and not

from small microdroplets carried away in the flow or other kinds of humidity effects (condensation at the aluminum surface etc.). For comparison, the experiment was carried out with deionised H_2^{16}O . The resulting spectra are depicted in Figure 4.10. Two band systems, showing a clearly recognisable shift of about one nanometer can be recognized. It must be kept in mind, that after the input of samples, also ambient air was introduced to the chamber. This required a previous purging with argon for at least 20 minutes to ensure least possible influence of ambient air. For spectral resolution of the emitted light the medium grating of the ICCD detector (1200 g/mm) was chosen. The resolving power of the chosen grating could therefore be considered as sufficient for following experiments, containing investigations on the isotope shift.

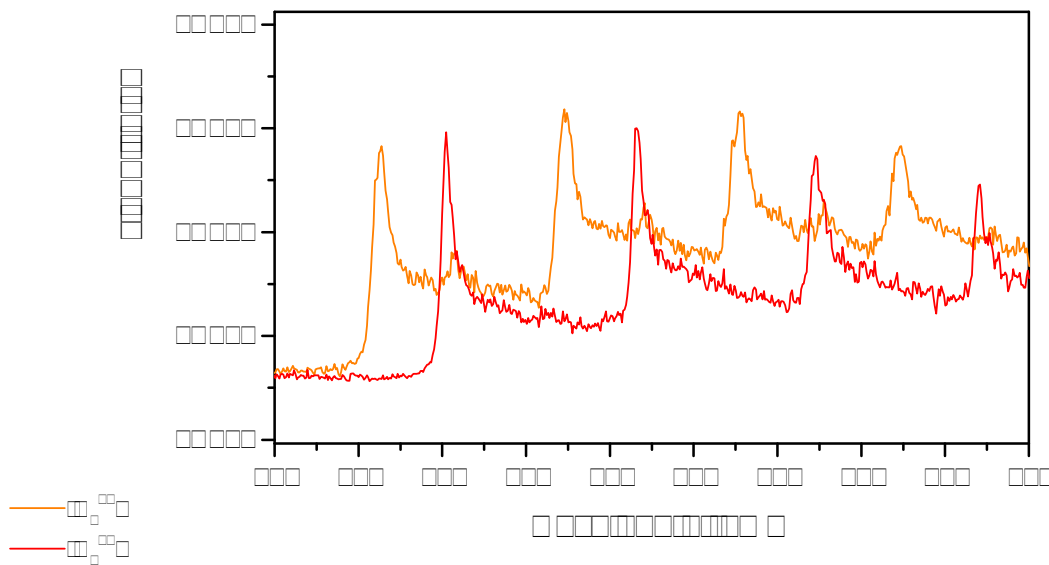


Figure 4.10: Comparison of the Al^{18}O (orange spectrum) and the Al^{16}O molecular emission (red spectrum). A clear shift of about one nanometer can be seen. Spectra were acquired at a gate delay of $5\ \mu\text{s}$ and a gate width of $5\ \mu\text{s}$. 200 shots were acquired. Detection was performed at the ICCD detector.

As the input of the water droplet to the chamber was unavoidably associated with a flushing of the chamber with ambient air, it was not possible to completely remove ambient oxygen from the atmosphere. Thus, small side-peaks can be seen in

the orange spectrum, originating from Al^{16}O molecular emission. Once inserted, a volume of $4\ \mu\text{L}$ allowed to enrich the atmosphere in the chamber for about 40 minutes with isotope labeled water. After 40 minutes a drastic decrease in the signal intensity of recorded Al^{18}O was noticed (see Figure 4.11). On this account, measurements were carried out after a purging period of 15 minutes after insertion of the droplet. To receive spectra of consistent quality, all spectra were recorded within 10 minutes.

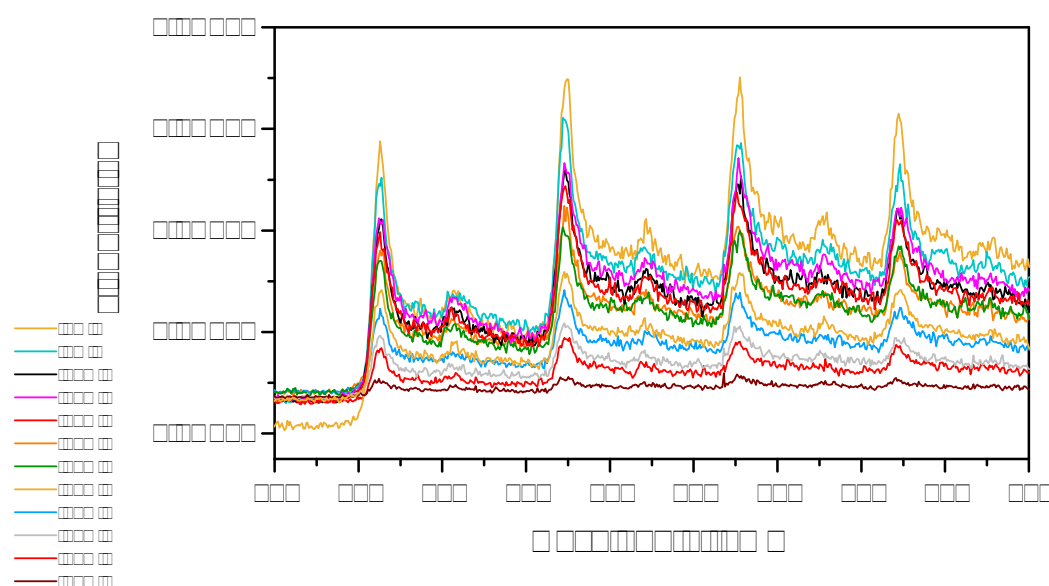


Figure 4.11: Temporal decrease of the signal intensity in observed AlO molecular emission bands. A stable signal can be seen between 15 and 35 minutes. After 40 minutes a significant reduction can be recognized.

For the construction of a calibration, two standard rows were measured in two separate experiment series. As in the experiment before, $4\ \mu\text{L}$ of sample liquid was placed in the chamber and a purging treatment was done, as described in the paragraph above. Six spectra were recorded for each point of the calibration row. For this measurements, the number of acquired shots was reduced to 100, to record six single spectra within a minute and therefore reduce the effect of decrease in H_2^{18}O saturation and allow equal conditions for each measurement.

Collected spectra were averaged and the Al¹⁸O bands were integrated after a baseline correction. An attempt was made to create a calibration curve by applying a partial least square (PLS) regression. The calibration curve was created with the first series of dilutions, containing content steps of 0; 10; 20; 30; 40; 50; 60; 70; 80; 90 and 100 %wt of H₂¹⁸O, by eliminating outliers and training the regression against the actual mass content values, which were known from the sample preparation.

To examine the quality of the created calibration, a second calibration row was prepared. For this data set, amounts of 0; 25; 50; 75 and 100 %wt H₂¹⁸O were chosen. The regression was following applied to the second data set. Again six spectra were recorded for each dilution step, to gain statistical certainty and eliminate outliers and avoid incorrect measurements. The averaged spectra are shown in Figure 4.12.

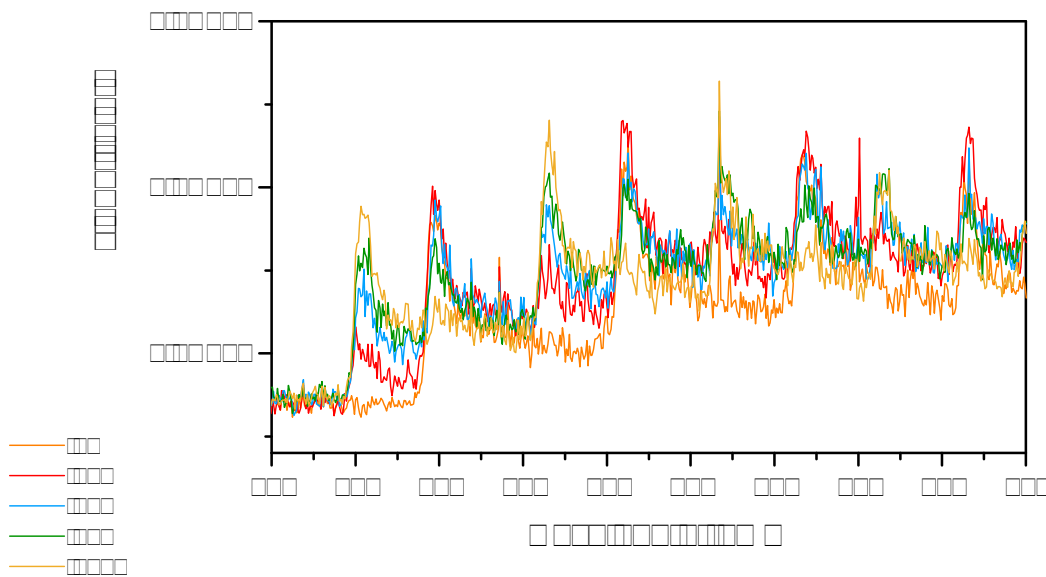


Figure 4.12: Averaged spectra from the measurements containing the saturation of the LIBS ablation chamber with H₂¹⁸O. For each dilution step six recorded spectra were merged.

The shown spectra give already a good idea of a linear trend. Following, the Al¹⁸O band was baseline corrected and integrated. The created calibration allowed to determine the mass content of H₂¹⁸O for the averaged spectrum for each dilution step

of the second calibration row from integrated peak areas. The resulting calculated mass content was plotted against the actual H_2^{18}O mass content for each dilution step. The actual mass contents were again known from the preparation of the calibration row (Figure 4.13).

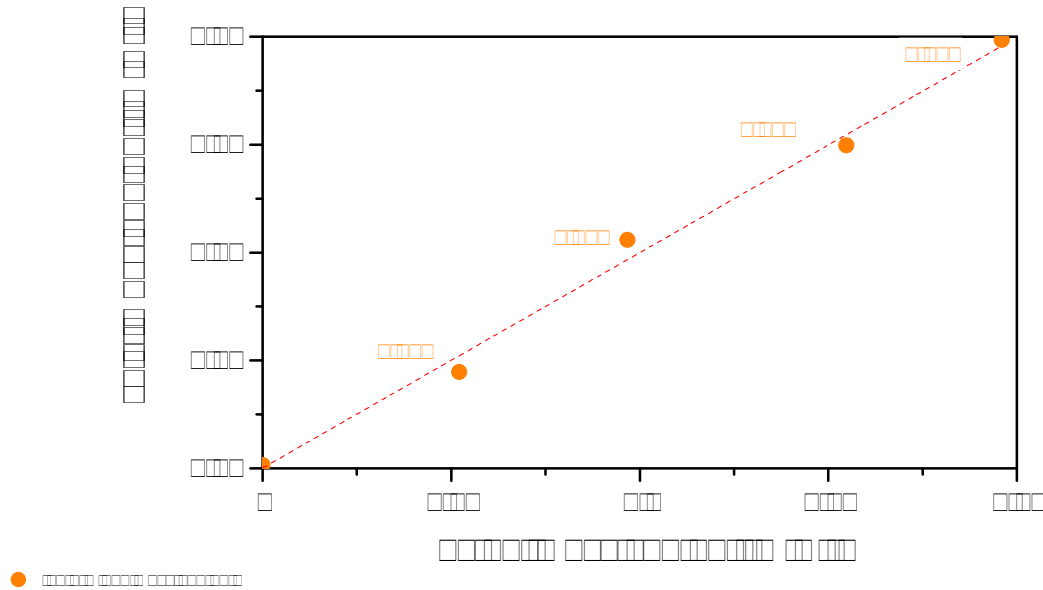


Figure 4.13: Plot of the calculated mass content values, plotted against the actual values. A good agreement between theoretical and actual values can be recognized.

The experimentally determined mass contents show a satisfying accordance to the actual content values. This is somewhat striking, due to the rather simple method. However, obtained findings clearly demonstrate that measurement of molecular AIO emissions allows not only a simple differentiation between ^{16}O and ^{18}O , but also quantitative assessment of the ^{18}O content in spiked water droplets.

4.4 Evaporation Measurements using the ETV

System

In experiments conducted so far, controlled evaporation of a certain volume of the prepared samples, and therefore the introduction of a defined volume of water to the ablation chamber was not possible. In further experiments, an ETV device was applied to achieve precisely controlled evaporation, employing a temperature program. A small volume was placed in the graphite boat and inserted in the graphite tube of the ETV. A temperature ramp was started and the resulting vapor phase was transported into the sample cell by means of an argon flow. In a first attempt, a row of spectra was collected, to estimate the width of the peak shaped profile, reaching the sample cell. 20 spectra were collected, directly following each other. For each spectrum, 50 shots were acquired. The low number of accumulated shots was chosen, to reach an appropriate fine subdivision of the time interval. The temperature program, overall lasted 60 seconds, with a ramp, lasting 40 seconds and a plateau at a temperature of 150°C, kept constantly for 20 seconds. The recording of the spectra took about 5 seconds per each, the whole measurement lasted 120 seconds, and thus covered the whole temperature ramp. The recording was started simultaneously with the temperature ramp. This allowed examining the development of the AIO Bands while introducing 10 μL of vaporized H_2^{18}O to the plasma. The recorded spectra are shown in [Figure 4.14](#).

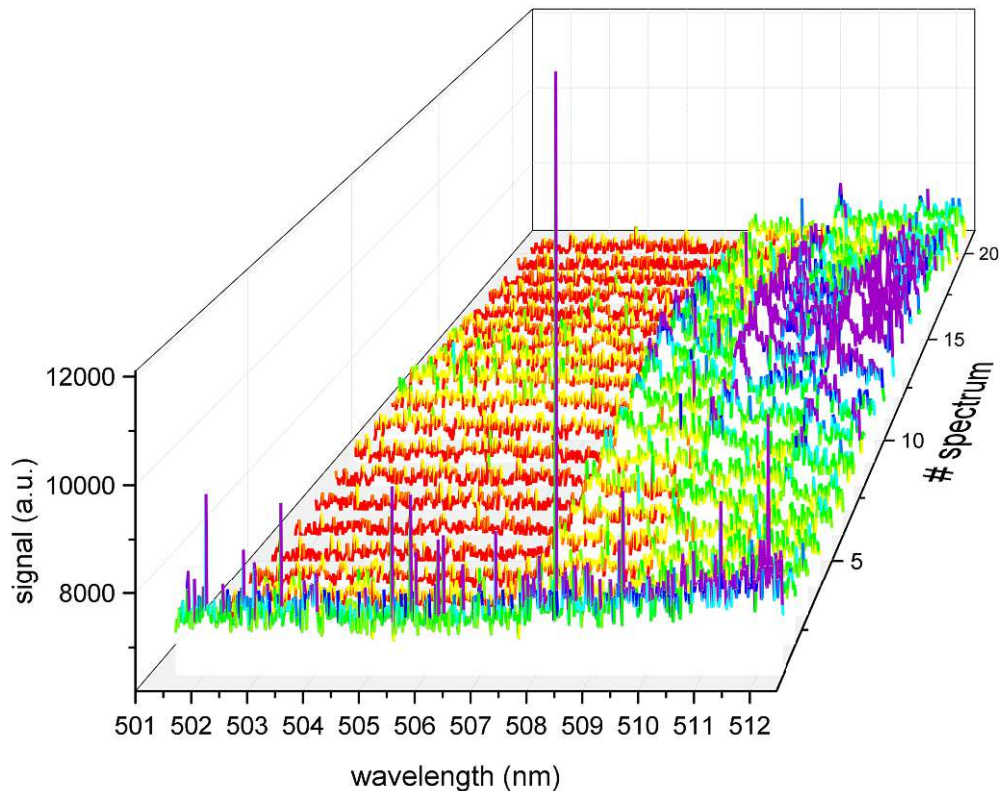


Figure 4.14: Evolution of the AIO band system in the course of time. 20 spectra of 50 shots per each were accumulated. At 507 nm the first significant band can be noticed at the sixth spectrum.

For a better overview of the temporal profile of the H_2^{18}O introduction to the ablation chamber, the maximum intensities of the AIO band at 509 nm in collected spectra shown in Figure 4.14 were read out and plotted against the corresponding time. The temporal development of the band is illustrated in Figure 4.15. First appearance of a notable AIO signal at 509 nm is recognized after 35 seconds.

The shown results demonstrate that the approach of using an ETV to introduce H_2O directly into the plasma plume works out, a significant change in signal intensities can be recognized. Afterwards, experiment parameters of the ETV were optimized. The goal was to achieve a quantitative transfer of the water vapor within a short time period and to record spectra showing a sufficient S/N.

The temperature program shown in Figure 3.7 was considered suitable for mea-

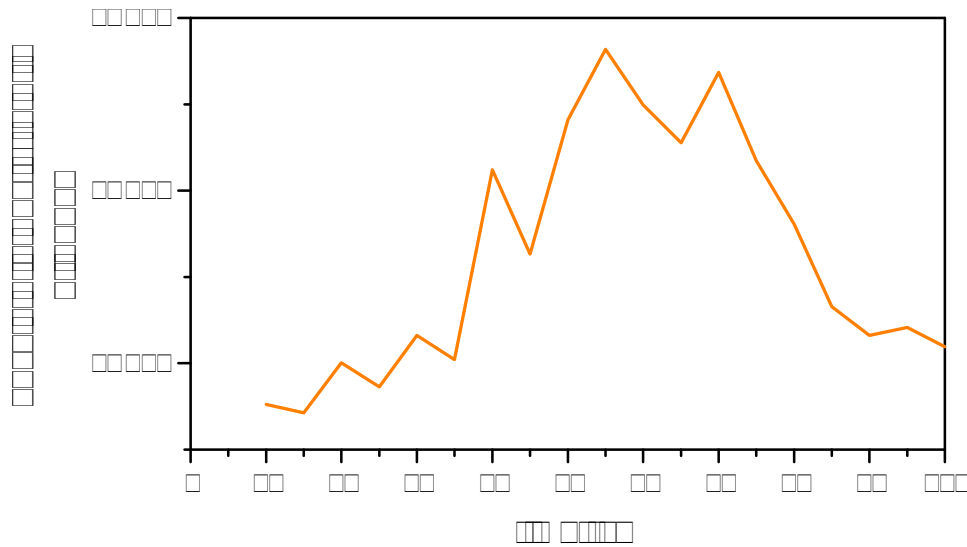


Figure 4.15: Development of the observed AIO band at 509 nm over time. The first significant signal can be detected after 35 seconds.

measurements on the evaporation of water. Due to the lack of notable AIO emission bands during the first 30 seconds, it can be ruled out, that significant amounts of vaporized sample are transferred to the cell and thus to the plasma. A large number of 1000 accumulated shots was chosen. At a repetition rate of 10 Hz this gives a duration of 100 seconds, allowing to cover the whole profile in Figure 4.15. Slower heat rates were not considered, as this would lead to even broader profiles and thus require even higher numbers of accumulated shots. A maximum temperature of 150°C can be seen as sufficient, as the samples were fully evaporated and a constant signal was observed at the end of the temperature program.

Having optimized the temperature program, the flow rate of the applied carrier gas flow was optimized next. As already stated in section 4.2 argon was chosen as gas for the transport of evaporated water. Both, carrier gas flow and bypass flow were varied. The results of the adjustment are shown in Figure 4.16.

Concerning the adjustment of the carrier gas flow, a flow rate of 200 mL per

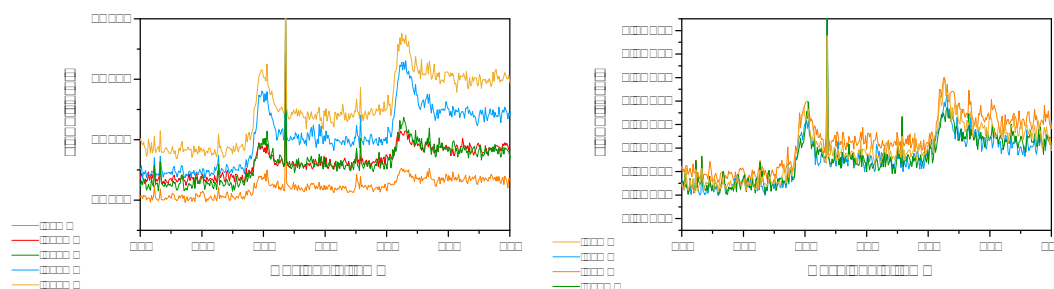


Figure 4.16: Left: adjustment of the carrier gas flow. A flow rate of 200 mL provides the best S/N ratio and suitable signal intensities. Higher flow rates result in a higher background. Right: Adjustment of the bypass gas flow. A flow rate of 100 mL per minute was chosen as the best bypass flow rate.

minute was identified as a suitable flow rate. Lower flow rates resulted in lower detectable signal intensities of the AIO bands. Higher flow rates lead to a decrease in the S/N and to a higher background in collected spectra. Following the flow rate of the carrier stream was reduced to 50 mL per minute to adapt the bypass flow. It is to be noted, that the bypass flow is not necessary for the described use of the ETV instrument. In conventional use of the instrument, the function of the bypass flow is to protect heat-sensitive ceramic components from high temperatures in the furnace. In this case, for one thing, a relatively low maximum temperature was applied and for the other, mentioned ceramic components were not included in the setup. Moreover, as the results shown in Figure 4.16 demonstrate, no significant effect of the bypass flow could be detected. Nevertheless, a low bypass flow was chosen, in order to minimize possible condensation effects inside the ETV. Following a carrier gas flow of 200 mL per minute and a bypass flow of 50 mL per minute was chosen for further experiments.

Based on this preliminary experiment, further investigations utilizing the ETV system for controlled introduction of water vapor into the sample cell were performed. Optimization of the flow parameters was carried out with H_2^{16}O . In the next step different volumes of H_2^{18}O were loaded into the graphite boat. Spectra were recorded at a gate delay of 1 μs and a gate width of 10 μs and a gain of 100 at

the ICCD detector. 1000 single shot spectra were recorded and accumulated. Sample volumes of 2, 5, 7 and 10 μL were loaded into the graphite boat. Resulting spectra are shown in Figure 4.17.

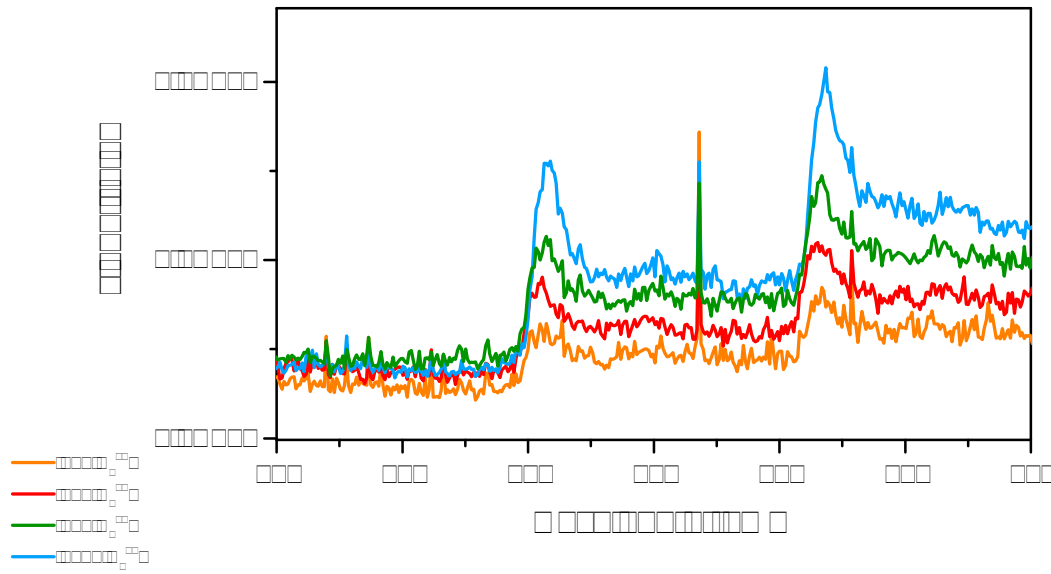


Figure 4.17: Recorded spectra after variation of the sample volume of H_2^{18}O . An increase in signal intensity is observed with increasing sample amounts.

Spectra presented in Figure 4.17 show an increasing signal intensity of the AlO bands with increasing amount of sample. The highest signal was recorded after evaporation of 10 μL of water. Subsequently, 10 μL of sample were evaporated for following measurements. Due to the limitation of the volume capacity of the graphite boat, the evaporation of higher volumes was restricted to this value.

At this point, it is necessary to discuss the laser matter interaction. As the laser proceeds with the ablation process, moving across the surface of the aluminum plate, following a pattern, it leaves behind a molten trace at the surface, slowly cooling down. Metallic aluminum has the property of instantaneously reacting with ambient oxygen, forming an oxide layer at the outmost surface. In our experiments, this leads to a loss in introduced water vapor being "consumed" by the aluminum.

During acquisition of spectra shown in [Figure 4.17](#) this effect was observed. If ablation takes place at the same location, a certain time after water was introduced, AlO molecular bands can still be observed. This behavior is shown in [Figure 4.18](#).

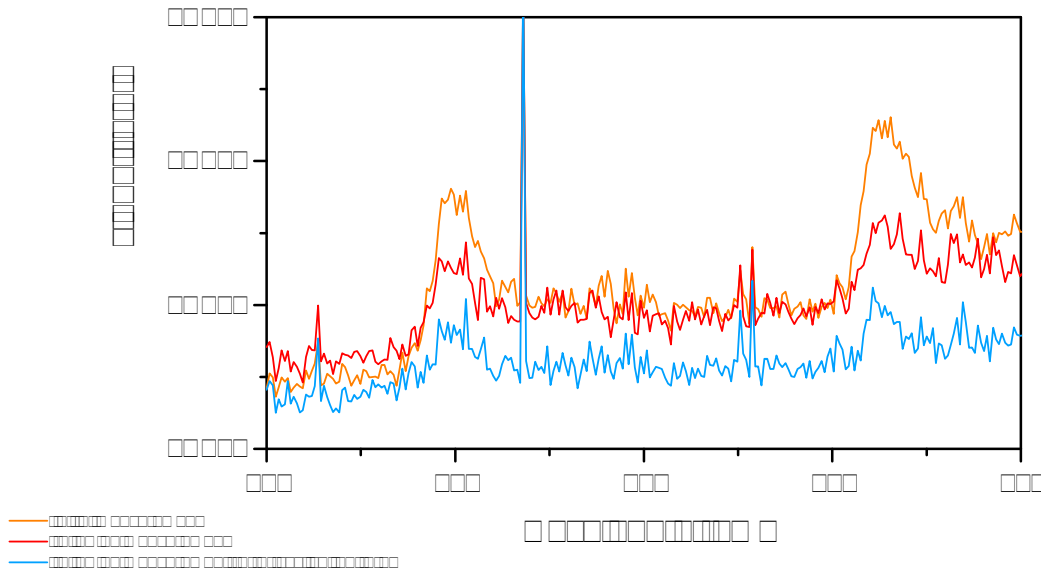


Figure 4.18: After a consecutive measurement 20 minutes after introducing $H_2^{18}O$ to the sample cell, corresponding $Al^{18}O$ bands can still be observed (red spectrum). Application of a cyclical pattern reduces formation of an $Al_2^{18}O_3$ layer at the aluminum surface (blue spectrum).

If an approximate complete transfer of the introduced oxygen content is aspired, this may become a problem. A possible way to circumvent this problem, is to create a cyclical pattern, repeatedly passing the same trace, and thus again transferring the formed $Al_2^{18}O_3$ layer into a plasma, leading to the wanted emission. A 4×4 mm hoof-shaped cyclical pattern was created, containing 200 shots spread over the course, being run through 5 times during one single measurement. This way, during every pass, a potentially formed aluminum oxide layer is continually ablated and transferred into the plasma. Thus, a reduced loss in ^{18}O can be assumed (see [Figure 4.18](#). The cyclical pattern is shown in [Figure 4.19](#)).

With optimized parameters, again an attempt was made to create a calibration. This time, mass contents of $H_2^{18}O$ of 0; 5; 10 and 20 %wt were chosen. This marks a

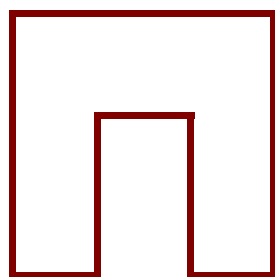


Figure 4.19: Cyclical hoof shaped pattern. 200 shots were spread over the pattern, which was consecutively run through 5 times, allowing to accumulate 1000 spectra in one measurement.

difference to the calibration attempt, discussed in [section 4.3](#), where dilution steps with H_2^{18}O mass contents between 0 and 100 %wt were chosen. The motivation behind this approach was to explore lower mass contents, as this comes closer to application problems, such as the absorption of water in polymers, which usually constitutes only a low fraction of the mass weight of a sample.

For each dilution step, a volume of 10 μL of the prepared sample was placed into the graphite boat. Again 1000 spectra were accumulated. All spectra were recorded at a gate delay of 1 μs and a gate width of 10 μs and a laser energy of 80% (about 3 mJ at the time of the measurement).

However, it turned out, that recording of a reliable and clear signal of AIO molecular emission was not detectable at this amounts. Also, no noteworthy band development was observed in a scan over the temperature program (see [Figure 4.20](#)).

As outlined, another range of the AIO blue-green system, whereas showed a very clear development of bands. The peak maximum of this AIO band lies at 484 nm, which is also described in literature (see [Figure 2.12](#) in [section 2.5](#)). Following attempts were made to create a calibration, applying this band for signal detection. Peak areas were integrated after baseline correction. Nevertheless, a linear regression model could not be detected, a direct connection between H_2^{18}O mass content in the sample and resulting signal in molecular emission bands was not observed. The averaged, resulting spectra of the calibration attempt are shown in [Figure 4.21](#).

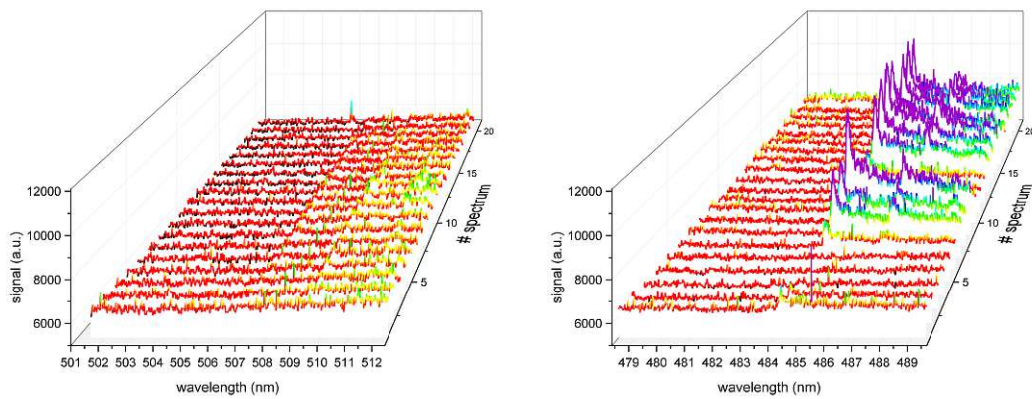


Figure 4.20: Evolution of the AIO band system in the course of time. 20 spectra of 50 shots per each were accumulated. The 10%wt dilution did not show a significant band development over time in the range between 501 and 512 nm (left). A different AIO band at 484 nm shows a very clear development of bands during the temperature program (right).

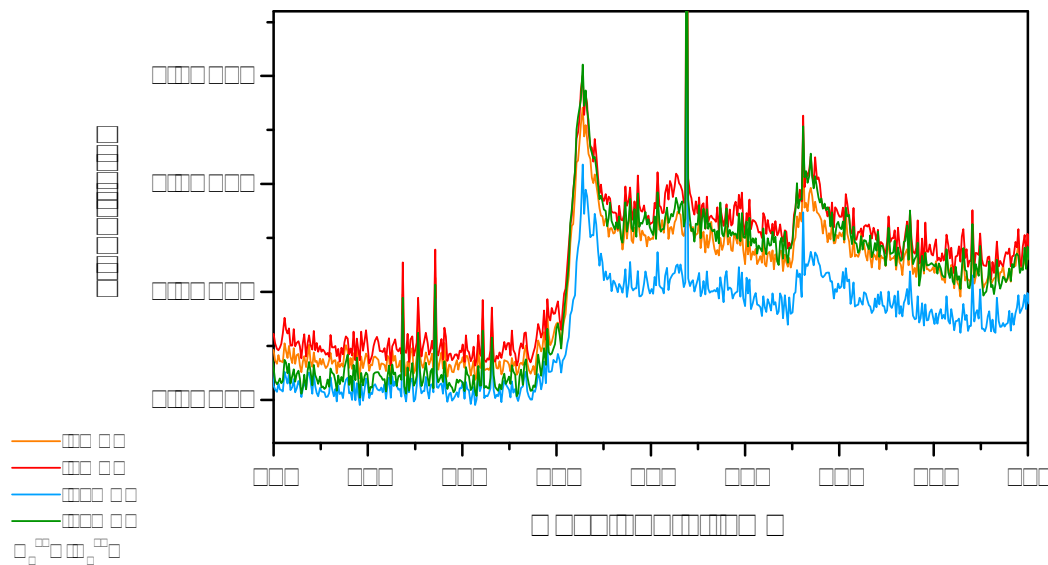


Figure 4.21: Averaged spectra of the calibration attempt at the AIO band at 484 nm. No relationship between introduced H_2^{18}O amounts and signal intensity could be observed.

Measurements were repeated, even setting the repetition rate of the laser to 20 Hz for once, to create a higher density of data collection points during the temperature profile. The changing of parameters was without success. Even a new created calibration row, diluting H_2^{18}O with MeCN instead of H_2^{16}O did not produce usable

results to create a calibration.

Finally, it can be stated, that presented experiments show that the concept of introducing a defined amount of H_2^{18}O to the LIBS plasma by evaporation applying an ETV instrument is possible, even if obtaining a quantifiable, proportional signal between the amount of introduced H_2^{18}O and molecular AIO emission did not succeed in the end.

4.5 Discussion of Problems

After all, it is not possible to give a particular reason for the failed calibration experiments. Although the proposed ETV approach for introduction of water vapor was found to be successful, no correlation between observed AIO signals and composition of the applied samples was found. Anyhow, some problems did occur during the experimental work in the laboratory, which may have led to these annoying results.

A major problem, which was already noted during the practical work, was a significant drop in the laser power, showing values lower than 1.5 mJ. Reasonable causes for this behavior were not found until now. An effect of the bad performance was a small spot, recognized at the surface of the dichroic mirrors, being properly burned into the glass surface. As a temporary solution, the dichroic mirrors were rotated, which led to a slightly better laser performance of about 2 mJ. To that must be added, that strong fluctuation of the laser power occurred between test days. This situation influenced all the pre-measurements. It was assumed, that a higher pulsing frequency would damage the special lens coating of the optical components of the device. On this account, the repetition rate of the laser was limited to 10 Hz or less. This was probably the biggest compromise, creating an upper limit for the time dependent evaporation measurements, leading to a longer time period between two consecutive shots. Long intervals between single shots can be viewed as counter-

productive, because no sample is transferred to a plasma during such a dead time, which results in a loss of sample. During a device service, the dichroic mirrors were changed, leading to an increase of the laser power to about 6 mJ. But again, the laser power decreased within some days to about 3.5 mJ, which was the determined laser power during the evaporation measurements using the ETV. This may indicate an improper operation of the laser. Laser performance was controlled by evaluation of the signal of a NIST 612 standard. The decay of the laser performance during the time of the experimental work is shown in Figure 4.22.

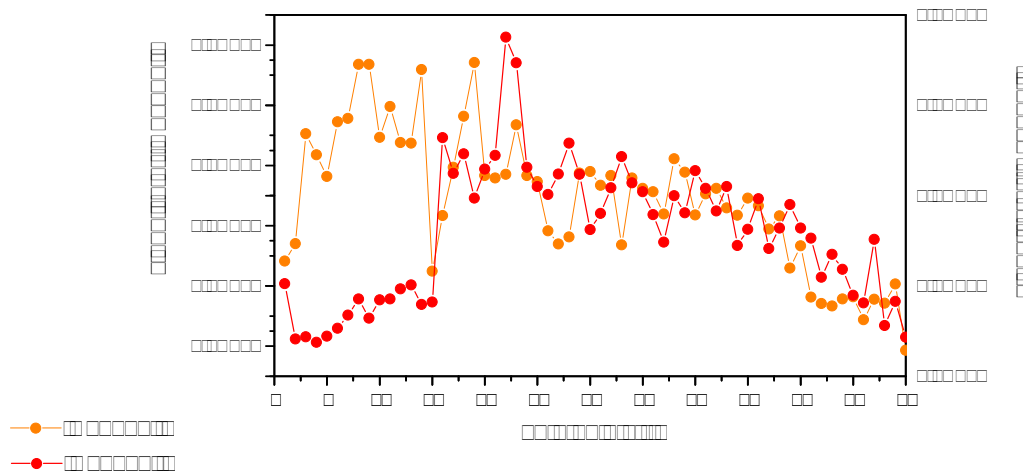


Figure 4.22: Decrease in laser power during measurement days. The laser power was determined every day before conducting measurements. Both shown channels of the CCD detector show a clear drop in signal intensity over time.

It must be mentioned that also a frequency of 20 Hz and a laser power of 6 mJ are by way of comparison, rather low values, with regard to the experimental goal of this work. Further effects, causing the failure of the experiments in section 4.4 can only be assumed. A possible reason could lie in the transport of the vaporized sample. Potential condensation effects in the unheated Teflon tube connecting the ETV and the sample cell could not be excluded. However, attempts have been made, to keep the transfer line as short as possible. Assumptions of suppressing effects, for example by the formation of other oxygen containing molecules, such as CO or

CO₂, can be excluded, due to the fact, that the H₂¹⁸O / H₂¹⁶O dilutions showed similar results to the H₂¹⁸O/MeCN system.

5 Conclusion and Outlook

In the presented work the isotopic shift in the AlO blue-green system was examined under various conditions. The AlO molecular emission band is of particular interest, given the fact, that oxygen isotopes are solely responsible for the resulting shift of the molecular bands. On contrary, aluminum as a mononuclidic element does not influence the band shift. In some applications, this may be of interest, especially for applications, including analysis of humidity in polymer films. This requires spatial resolved analysis and depth information, which are common applications for LIBS. The main part of this work focused on examining a new technique, wherein isotope labeled water was vaporized and introduced to the gas phase. For this purpose, a conventional LIBS instrument was combined with an ICCD detection system. This comparable simple setup allowed direct analysis of the samples. The analysis of prepared AlN/Al₂O₃ pellets showed the suitability of the chosen setup to resolve the AlO molecular emission bands in recorded spectra. In further experiments, it could be shown, that the signal intensity depends on the ratio between aluminum and oxygen contents in the sample. An increase in the signal intensities was observed at oxygen excess.

The saturation of the atmosphere inside the ablation chamber with water vapor, allowed to demonstrate the feasibility of external introduction of H₂O direct into a LIP, generated on a metallic aluminum plate. Application of H₂¹⁸O resulted in a pronounced isotopic shift of the molecular emission bands of the isotopologues Al¹⁸O and Al¹⁶O. An approach for calibration was to prepare a set of different standards

with varying contents of H_2^{18}O . The environment of a metallic aluminum sample was again saturated with vapor from the produced standards and thus introduced to a laser induced plasma on the aluminum sample. It was possible to obtain a calibration by data evaluation using a PLS method. A second set of standards with different contents of H_2^{18}O was measured for validation of the proposed method. Integration of the obtained peak areas and quantification using the determined calibration function resulted in H_2^{18}O contents which were in good agreement with the actual contents, known from the preparation of the dilutions.

After feasibility of this approach has been demonstrated for the analysis of solid samples, the procedure has been adopted for the measurement of water vapor. To improve the evaporation of aqueous standards, an ETV system was connected to the ablation chamber and a timed program was executed, allowing to transfer introduced samples as completely as possible to the plasma. Observed signals indicated formation of AlO - thus feasibility of proposed approach could be demonstrated.

Compared to the previous approach, this ETV procedure allowed a controlled evaporation and transfer of heavy water could be accomplished – a prerequisite for quantitative measurements.

However, between the observed AlO emission intensities and the applied H_2^{18}O contents no correlation was found. The resulting data did not follow a linear regression model. Possible reasons for the failure can be found in the deteriorating laser performance and the repetition rate limitations of the used instrument.

A possible approach to achieve a better laser performance, is to work at a different wavelength of the Nd:YAG laser. As mentioned in [subsection 2.3.2](#) a wavelength of 266 nm is obtained by fourfold frequency multiplication, by means of a dichroic system. Frequency multiplication inevitably involves a loss of energy in every multiplication step, as only a part of the laser beam is frequency multiplied and then filtered by means of a dichroic mirror. The filtering of a spectral range is accompa-

nied by the loss of energy of respective spectral components. In literature the use of other Nd:YAG lasers is well reported. Operating at the ground frequency (1064 nm) or the first harmonics (532 nm) for example is connected with a higher laser power and thus better excitation. Short wavelengths are usually applied if better ablation properties and ionization rates are needed. The application of a 532 nm Nd:YAG could therefore lead to better excitation and better signal generation in molecular LIBS [56][57][58].

Eventually, the limited repetition rate of 10 Hz by the applied Nd:YAG laser has proven to be insufficient. At a given pulse duration of 6 ns, a repetition rate of 10 Hz yields in an actual time span of 60 ns, in which excitation occurs. During the remaining "dead time", no sample is transferred to a plasma plume. This marks an extensive loss of analyte in intervals between laser pulses. In literature the use of kHz and also MHz Nd:YAG lasers is reported [59][60][61]. Application of such repetition rates would allow to acquire a much higher number of spectra, within a shorter time frame, making observation of more data points, along a profile of introduced H₂O as described above, possible. Perhaps, this could help to further develop the shown concept and make quantification of the AIO signal feasible.

List of Figures

2.1	The emission process. Energy from an external source leading to an excitation of a valence electron. The relaxation of such excited states is accompanied by the emission of a photon, with a frequency ν , corresponding to the energy difference between excited state and ground state [40].	9
2.2	Different time regimes in the evolution of the plasma. The signal intensity reaches its maximum while the laser pulse is still enduring. Following, excited states start to collapse (breakdown). The gate delay (GD) marks the time interval between the onset of the laser pulse and the measurement. The measurement covers a certain time interval, defined by the gate width (GW). The gate width is adjusted by the ICCD detector by means of a detector gate pulse, which allows to trigger the passage of a wanted signal and to ignore unwanted signals. Short gate delays (10 ns) provide a large background and poorly resolved signals. Optimized gate delays (1 μ s) show well resolved signals but absolute signal intensities decrease. However, a higher S/N ratio is observed. Recreation from [49][50]	12
2.3	Schematic principle of a dichroic mirror (left, recreated from [33]) and experimental setup of a LIBS apparatus (right)[34].	15
2.4	Schematic layout of a Nd:YAG laser. A flashlight is implemented, working as an optical pump [34].	17

2.5	Drawing of an (a) (c) flashlamp pumped, (b) diode pumped Nd:YAG Laser [48][33].	18
2.6	Wavelength selection in the Czerny-Turner arrangement (left) [33] and schematic drawing of a grating (right). Dispersed light beams leave the grating at different angles. The Blaze-angle is marked in an extension axis of a grating-tooth [34].	23
2.7	The arrangement of a typical echelle monochromator. Wavelength separation is performed by two dispersive elements: a prism and a grating. A two-dimensional plot of separated dispersing orders is schematically shown at the detector plane [33].	24
2.8	A side-on PMT (left) and a head-on PMT (right). The electron cascade is drawn yellow [53].	26
2.9	Setup of a CCD chip [54]. The precisely timed driving voltage pulse is applied by a register clock control.	28
2.10	Schematic setup of a typical ICCD chip. Angled channels in the MCP can be seen. Heat development at the CCD during photon registration and signal processing is countered by a Peltier cooling-element [33].	29
2.11	The Al ¹⁶ O blue-green system. The five subsystems are clearly visible [55].	30
2.12	LIBS spectrum of the peak at 507 nm. The spectra were acquired with 20 μs gate delay. 100 spectra were accumulated [37].	31
3.1	The chosen LIBS setup consisting of a LIBS instrument, an external spectrometer and an ETV apparatus. Top right: the beam path inside the LIBS instrument (top view) is shown. (a) power and coolant supply (b) laser (c) harmonics (d) dichroics (e) attenuator (f) adjustable mirror (h) aperture (i) collection optics.	34

- 3.2 The drawer, containing a Teflon inlet. Solid samples are placed in the recess of the inlet (left). A holder made from aluminum and the sample cell used for measurements applying the ETV instrument, containing a cover, a screw bolt connection, a quartz window, a viton seal (right). 36
- 3.3 Inside of the ETV. (a) bypass argon flow, (b) Teflon tube connected to the sample cell (see Figure 3.2), (c) cooled brackets, (d) graphite boat, (e) carrier argon flow, (f) connection cable to a thermoelement for temperature control, (g) graphite furnace. 37
- 3.4 A meander pattern (left) and a point pattern (right). 39
- 3.5 Arrangement used for water enrichment of an argon flow. 40
- 3.6 Schematic view of the $H_2^{18}O$ droplet on the aluminum surface, protected by a Teflon ring. 40
- 3.7 The temperature program for measurements containing evaporation of water by means of the ETV. Within 40 seconds a temperature of $150^\circ C$ was reached, which was held constantly for 20 seconds before cooling down to room temperature again. 41
- 4.1 Finding of experiment parameters at the CCD detector. Initial values can be found in Table 3.1. Top left: adjustment of gate delays. Top right: influence of the laser energy on the signal intensity. Below left: influence of the different amounts of shots. Below right: optimized signal collection. A gate delay of $1 \mu s$, a laser energy of 80% and a number of 200 shots were found as suitable parameters. 44

- 4.2 Recorded spectra under ambient air (red) and argon atmosphere (orange). A small gate delay of 0.2 μs was chosen, to detect even small amounts of formed AIO. Detection was made at the ICCD detector, to take full advantage of the better sensitivity. The gain was set to 100, a gate width of 10 μs was chosen. A small spotsize of 100 μm was set to ensure high irradiance. Under argon atmosphere Peaks at 507, 510, 512 and 514 nm disappear, hinting the absence of AIO formation in the plasma. 45
- 4.3 Fine adjustment of gate delay at an Al_2O_3 pellet, showing a decrease in absolute signal intensity at larger gate delays. 46
- 4.4 Development of AIO molecular emission under different atmospheres. Helium clearly suppresses signal development of discussed AIO emission bands. 200 shots were acquired at a gate delay of 1 μs and a gate width of 10 μs 48
- 4.5 Different signal intensities in recorded spectra of the set of $\text{Al}_2\text{O}_3/\text{Al}$ pellets, showing an increasing trend as the amount of oxygen in the sample increases. Measurement took place at a gate delay of 0.7 μs at the CCD detector. 500 shots were acquired in both spectra. 49
- 4.6 Different signal intensities of one single band (left) and the whole band system (right) at different oxygen contents in the $\text{Al}_2\text{O}_3/\text{AlN}$ pellets. 200 shots were accumulated at a gate delay of 1 μs and a gate width of 10 μs . Detection was performed at the ICCD detector. 50
- 4.7 Read out peak heights (left) and integrated peak areas (right) plotted against molar fractions of oxygen in the sample pellets. An increase in signal intensity with increasing oxygen amount can be observed. 51
- 4.8 Development of the AIO band at 507 nm under dry argon atmosphere without saturation of water (red spectrum) and under the influence of an argon flow loaded with water (orange spectrum) and under ambient conditions (blue spectrum). 52

- 4.9 After flushing the chamber with argon (2L min⁻¹) for 5 minutes the influence of introduced vapor can no longer be recognized, leaving behind signals that provide a constant background. A gate delay of 1 μ s was chosen, 150 shots were accumulated. 54
- 4.10 Comparison of the Al¹⁸O (orange spectrum) and the Al¹⁶O molecular emission (red spectrum). A clear shift of about one nanometer can be seen. Spectra were acquired at a gate delay of 5 μ s and a gate width of 5 μ s. 200 shots were acquired. Detection was performed at the ICCD detector. 55
- 4.11 Temporal decrease of the signal intensity in observed AIO molecular emission bands. A stable signal can be seen between 15 and 35 minutes. After 40 minutes a significant reduction can be recognized. . . . 56
- 4.12 Averaged spectra from the measurements containing the saturation of the LIBS ablation chamber with H₂¹⁸O. For each dilution step six recorded spectra were merged. 57
- 4.13 Plot of the calculated mass content values, plotted against the actual values. A good agreement between theoretical and actual values can be recognized. 58
- 4.14 Evolution of the AIO band system in the course of time. 20 spectra of 50 shots per each were accumulated. At 507 nm the first significant band can be noticed at the sixth spectrum. 60
- 4.15 Development of the observed AIO band at 509 nm over time. The first significant signal can be detected after 35 seconds. 61
- 4.16 Left: adjustment of the carrier gas flow. A flow rate of 200 mL provides the best S/N ratio and suitable signal intensities. Higher flow rates result in a higher background. Right: Adjustment of the bypass gas flow. A flow rate of 100 mL per minute was chosen as the best bypass flow rate. 62

- 4.17 Recorded spectra after variation of the sample volume of H_2^{18}O . An increase in signal intensity is observed with increasing sample amounts. 63
- 4.18 After a consecutive measurement 20 minutes after introducing H_2^{18}O to the sample cell, corresponding Al^{18}O bands can still be observed (red spectrum). Application of a cyclical pattern reduces formation of an $\text{Al}_2^{18}\text{O}_3$ layer at the aluminum surface (blue spectrum). 64
- 4.19 Cyclical hoof shaped pattern. 200 shots were spread over the pattern, which was consecutively run through 5 times, allowing to accumulate 1000 spectra in one measurement. 65
- 4.20 Evolution of the AIO band system in the course of time. 20 spectra of 50 shots per each were accumulated. The 10%wt dilution did not show a significant band development over time in the range between 501 and 512 nm (left). A different AIO band at 484 nm shows a very clear development of bands during the temperature program (right). 66
- 4.21 Averaged spectra of the calibration attempt at the AIO band at 484 nm. No relationship between introduced H_2^{18}O amounts and signal intensity could be observed. 66
- 4.22 Decrease in laser power during measurement days. The laser power was determined every day before conducting measurements. Both shown channels of the CCD detector show a clear drop in signal intensity over time. 68

List of Tables

3.1	Initial LIBS parameters for premeasurements concerning pellets . . .	38
3.2	Parameters of the premeasurements containing evaporation of water.	40
3.3	Parameters of the premeasurements containing evaporation of water using the ETV	42
.1	Preparation of Al/Al ₂ O ₃ Pellets	80
.2	Preparation of AlN/Al ₂ O ₃ Pellets	80
.3	Preparation of a H ₂ ¹⁸ O/H ₂ ¹⁶ O dilution row (dilution steps: 25%wt) . .	80
.4	Preparation of a H ₂ ¹⁸ O/H ₂ ¹⁶ O dilution row (dilution steps: 10%wt) . .	81
.5	Preparation of a H ₂ ¹⁸ O/H ₂ ¹⁶ O dilution row for experiments containing ETV evaporation	82
.6	Preparation of a H ₂ ¹⁸ O/MeCN dilution row for experiments contain- ing ETV evaporation	82

Appendix

Table .1: Preparation of Al/Al₂O₃ Pellets

m (g)	1:1	2:1	5:1
Al ₂ O ₃	0.8673	0.5101	0.2348
Al	0.2289	0.5396	0.8066
Σ	1.0974	1.0497	1.0414

Table .2: Preparation of AlN/Al₂O₃ Pellets

m (g)	AlN	10:1	6:1	5:1	4:1	2:1	4:3	1:1	4:5	Al ₂ O ₃
Al ₂ O ₃	0.0000	0.0921	0.1273	0.1833	0.2034	0.4582	0.611	0.8175	1.024	1.1093
AlN	1.1045	1.0327	0.9218	0.9591	0.8205	0.7373	0.4922	0.3274	0.1651	0.0000
Σ	1.1045	1.1248	1.0491	1.1424	1.0239	1.1955	1.1032	1.1449	1.1891	1.1093

Table .3: Preparation of a H₂¹⁸O/H₂¹⁶O dilution row (dilution steps: 25%wt)

m (mg)	0%wt	25%wt	50%wt	75%wt	100%wt
H ₂ ¹⁸ O	0	24	22	74	21
H ₂ ¹⁶ O	540	78	21	25	0
Σ	540	102	43	99	21

Table .4: Preparation of a $H_2^{18}O/H_2^{16}O$ dilution row (dilution steps: 10%wt)

m (mg)	0 %wt	10%wt	20%wt	30%wt	40%wt	50%wt	60%wt	70%wt	80%wt	90%wt	100%wt
$H_2^{18}O$	0	11	22	27	41	44	57	72	79	92	21
$H_2^{16}O$	221	91	79	66	62	48	39	34	18	11	0
Σ	221	102	101	93	103	92	96	106	97	103	21

Table .5: Preparation of a $H_2^{18}O/H_2^{16}O$ dilution row for experiments containing ETV evaporation

m (mg)	0 %wt	5%wt	10%wt	15%wt	20%wt
$H_2^{18}O$	0	6	11	17	22
$H_2^{16}O$	540	95	86	83	75
Σ	540	101	97	100	97

Table .6: Preparation of a $H_2^{18}O/MeCN$ dilution row for experiments containing ETV evaporation

m (mg)	0 %wt	5%wt	10%wt	20%wt
$H_2^{18}O$	0	7	12	21
MeCN	650	92	83	77
Σ	650	99	95	98

Bibliography

- [1] Sies. H. “Role of reactive oxygen species in biological processes.” In: *Klinische Wochenschrift* 69.21-23 (1991), pp. 965–968.
- [2] Bryan C Dickinson and Christopher J Chang. “Chemistry and biology of reactive oxygen species in signaling or stress responses.” In: *Nature chemical biology* 7.8 (2011), pp. 504–511.
- [3] Victoria S. Meadows et al. “Exoplanet Biosignatures: Understanding Oxygen as a Biosignature in the Context of Its Environment.” In: *Astrobiology* 18.6 (2018), pp. 630–662.
- [4] Roghieh Hajiboland. “Chapter 1 Reactive Oxygen Species and Photosynthesis.” In: *Oxidative Damage to Plants*. Ed. by Parvaiz Ahmad. San Diego: Academic Press, 2014, pp. 1–63. ISBN: 978-0-12-799963-0.
- [5] Semenza Gregg L. “Life with oxygen.” In: *Science* 318.5847 (2007), pp. 62–64.
- [6] Avnish Kumar Arora et al. “Applications of metal/mixed metal oxides as photocatalyst:(A review).” In: *Oriental Journal of Chemistry* 32.4 (2016), p. 2035.
- [7] B.C.H. Steele. “Oxygen ion conductors and their technological applications.” In: *Materials Science and Engineering B* 13.2 (1992), pp. 79–87. ISSN: 0921-5107. URL: <https://www.sciencedirect.com/science/article/pii/092151079290146Z>.
- [8] Jose Luis G Fierro. *Metal oxides: chemistry and applications*. CRC press, 2005.

- [9] E. Fritz and W. Gebert. “Milestones and challenges in oxygen steelmaking.” In: *Revue de Métallurgie* 102.1 (2005), pp. 33–49. doi: [10.1051/metal:2005172](https://doi.org/10.1051/metal:2005172).
- [10] S Greenfield, H McD McGeachin, and PB Smith. “Plasma emission sources in analytical spectroscopy—I.” In: *Talanta* 22.1 (1975), pp. III–IV.
- [11] Velmer A Fassel. “Current and potential applications of inductively coupled plasma (ICP)-atomic emission spectroscopy (AES) in the exploration, mining, and processing of materials.” In: *Analytical Chemistry in the Exploration, Mining and Processing of Materials* (1978), pp. 1533–1545.
- [12] T Charng and F Lansing. “Review of corrosion causes and corrosion control in a technical facility.” In: *TDA progress report* 42.69 (1982), pp. 145–156.
- [13] Helmut Kaesche. *Corrosion of metals: physicochemical principles and current problems*. Springer Science and Business Media, 2012.
- [14] CM Hansson. “The impact of corrosion on society.” In: *Metallurgical and Materials Transactions A* 42.10 (2011), pp. 2952–2962.
- [15] Vladimir Neburchilov et al. “A review of polymer electrolyte membranes for direct methanol fuel cells.” In: *Journal of Power Sources* 169.2 (2007), pp. 221–238.
- [16] Xiaolong Li, Kai Han, and Yu Song. “Dynamic behaviors of PEM fuel cells under load changes.” In: *International Journal of Hydrogen Energy* 45.39 (2020). The 7th International Conference on Energy, Engineering and Environmental Engineering, pp. 20312–20320. ISSN: 0360-3199. doi: <https://doi.org/10.1016/j.ijhydene.2019.12.034>. URL: <https://www.sciencedirect.com/science/article/pii/S0360319919345343>.
- [17] Rod Borup et al. “Scientific aspects of polymer electrolyte fuel cell durability and degradation.” In: *Chemical reviews* 107.10 (2007), pp. 3904–3951.

- [18] David S Soane and Zoya Martynenko. “Polymers in Microelectronics.” In: (1989).
- [19] T. Liang, Y. Makita, and S. Kimura. “Effect of film thickness on the electrical properties of polyimide thin films.” In: *Polymer* 42.11 (2001), pp. 4867–4872. ISSN: 0032-3861. DOI: [https://doi.org/10.1016/S0032-3861\(00\)00881-8](https://doi.org/10.1016/S0032-3861(00)00881-8). URL: <https://www.sciencedirect.com/science/article/pii/S0032386100008818>.
- [20] R. Buchhold et al. “Influence of Moisture-Uptake on Mechanical Properties of Polymers Used in Microelectronics.” In: *MRS Proceedings* 511 (1998), p. 359. DOI: [10.1557/PROC-511-359](https://doi.org/10.1557/PROC-511-359).
- [21] Xinran Qin et al. “Characterization of Hygroscopic Insulator Contamination via Laser-Induced Breakdown Spectroscopy.” In: *IEEE Transactions on Plasma Science* 49.3 (2021), pp. 1166–1172. DOI: [10.1109/TPS.2021.3051336](https://doi.org/10.1109/TPS.2021.3051336).
- [22] Maria Francesca Alberghina et al. “Integrated analytical methodologies for the study of corrosion processes in archaeological bronzes.” In: 66.2 (), pp. 129–137. ISSN: 0584-8547. DOI: <https://doi.org/10.1016/j.sab.2010.12.010>. URL: <https://www.sciencedirect.com/science/article/pii/S0584854710003381>.
- [23] Jian Zhang et al. “Chemical analysis of the initial corrosion layer on pipeline steels in simulated CO₂-enhanced oil recovery brines.” In: *Corrosion Science* 65 (2012), pp. 397–404. ISSN: 0010-938X. DOI: <https://doi.org/10.1016/j.corsci.2012.08.045>. URL: <https://www.sciencedirect.com/science/article/pii/S0010938X12004003>.
- [24] Stefano Legnaioli et al. “Applications of LIBS to the Analysis of Metals.” In: *Laser-induced breakdown spectroscopy*. Springer, 2014, pp. 169–193.
- [25] C Bas and ND Alberola. “Dynamic mechanical behavior of poly (aryl ether ether ketone) in the- 150° C to+ 100° C temperature range: Influence of the na-

- ture of sorbed solvents.” In: *Polymer Engineering & Science* 36.2 (1996), pp. 244–253.
- [26] John Mitchell. “Methods for the determination of water in polymers.” In: *Analytica Chimica Acta* 81.2 (1976), pp. 231–263. ISSN: 0003-2670. DOI: [https://doi.org/10.1016/S0003-2670\(01\)82024-9](https://doi.org/10.1016/S0003-2670(01)82024-9). URL: <https://www.sciencedirect.com/science/article/pii/S0003267001820249>.
- [27] Amir Hossein Farhadian et al. “A novel approach for investigation of chemical aging in composite propellants through laser-induced breakdown spectroscopy (LIBS).” In: *Journal of Thermal Analysis and Calorimetry* 124.1 (2016), pp. 279–286.
- [28] J Varlet et al. “Dynamic mechanical spectrometry of nylon-12.” In: *Journal of Polymer Science Part B: Polymer Physics* 28.13 (1990), pp. 2691–2705.
- [29] G Baschek, G Hartwig, and F Zahradnik. “Effect of water absorption in polymers at low and high temperatures.” In: *Polymer* 40.12 (1999), pp. 3433–3441. ISSN: 0032-3861. DOI: [https://doi.org/10.1016/S0032-3861\(98\)00560-6](https://doi.org/10.1016/S0032-3861(98)00560-6). URL: <https://www.sciencedirect.com/science/article/pii/S0032386198005606>.
- [30] SA Walker et al. “Oxygen isotope measurements of seawater (18O/16O): A comparison of cavity ring-down spectroscopy (CRDS) and isotope ratio mass spectrometry (IRMS).” In: *Limnology and Oceanography: Methods* 14.1 (2016), pp. 31–38.
- [31] Christophe Lécuyer et al. “High-precision determination of 18O/16O ratios of silver phosphate by EA-pyrolysis-IRMS continuous flow technique.” In: *Journal of Mass Spectrometry* 42.1 (2007), pp. 36–41. DOI: <https://doi.org/10.1002/jms.1130>. eprint: <https://analyticalsciencejournals.onlinelibrary.wiley.com/doi/pdf/10.1002/jms.1130>. URL: <https://analyticalsciencejournals.onlinelibrary.wiley.com/doi/abs/10.1002/jms.1130>.

- [32] U Hener et al. “Simultaneous on-line analysis of $^{18}\text{O}/^{16}\text{O}$ and $^{13}\text{C}/^{12}\text{C}$ ratios of organic compounds using GC-pyrolysis-IRMS.” In: *Zeitschrift für Lebensmitteluntersuchung und-Forschung A* 206.3 (1998), pp. 230–232.
- [33] Reinhard Noll. “Laser-induced breakdown spectroscopy.” In: *Laser-Induced Breakdown Spectroscopy*. Springer, 2012, pp. 7–15.
- [34] Sergio Musazzi and Umberto Perini. “Laser-induced breakdown spectroscopy.” In: *Springer Series in Optical Sciences* 182 (2014).
- [35] James Derosé and Kay Scheffler. “Rapid, Accurate Materials Analysis with a 2-Methods-In-1 Solution.” In: *Quality* 58.13 (2019), pp. 21–24.
- [36] S. Messaoud Aberkane et al. “Depth profiling of alumina thin films using laser induced breakdown spectroscopy: Structural and morphological dependence.” In: *Thin Solid Films* 653 (2018), pp. 293–300. ISSN: 0040-6090. DOI: <https://doi.org/10.1016/j.tsf.2018.03.052>. URL: <https://www.sciencedirect.com/science/article/pii/S0040609018301962>.
- [37] Alexander A Bol’shakov et al. “Laser ablation molecular isotopic spectrometry (LAMIS): current state of the art.” In: *Journal of Analytical Atomic Spectrometry* 31.1 (2016), pp. 119–134.
- [38] URL: https://physics.nist.gov/cgi-bin/Compositions/stand_alone.pl.
- [39] Karl Cammann. *Instrumentelle Analytische Chemie: Verfahren, Anwendungen und Qualitätssicherung*. Spektrum Akademischer Verlag Heidelberg, 2010.
- [40] Manfred H Gey. “Atomspektroskopie.” In: *Instrumentelle Analytik und Bioanalytik*. Springer, 2021, pp. 259–284.
- [41] Michel Piette, Bernard Desmet, and Richard Dams. “Determination of strontium in human whole blood by ICP-AES.” In: *Science of The Total Environment* 141.1 (1994), pp. 269–273. ISSN: 0048-9697. DOI: <https://doi.org/>

- 10 . 1016 / 0048 - 9697(94) 90033 - 7. URL: <https://www.sciencedirect.com/science/article/pii/0048969794900337>.
- [42] James M Harrington et al. “Analysis of human serum and whole blood for mineral content by ICP-MS and ICP-OES: development of a mineralomics method.” In: *Biological trace element research* 160.1 (2014), pp. 132–142.
- [43] AP Rowland and PM Haygarth. *Determination of total dissolved phosphorus in soil solutions*. Tech. rep. Wiley Online Library, 1997.
- [44] R Rubio, J Huguet, and G Rauret. “Comparative study of the Cd, Cu and Pb determination by AAS and by ICP-AES in river water: Application to a mediterranean river (Congost river, Catalonia, Spain).” In: *Water Research* 18.4 (1984), pp. 423–428. ISSN: 0043-1354. DOI: [https://doi.org/10.1016/0043-1354\(84\)90149-0](https://doi.org/10.1016/0043-1354(84)90149-0). URL: <https://www.sciencedirect.com/science/article/pii/0043135484901490>.
- [45] SE Silliman et al. “Observations on elemental concentrations of groundwater in central Benin.” In: *Journal of Hydrology* 335.3-4 (2007), pp. 374–388.
- [46] Abua Ikem et al. “Chemical quality of bottled waters from three cities in eastern Alabama.” In: *Science of the total environment* 285.1-3 (2002), pp. 165–175.
- [47] M Tighe et al. “Comparison of digestion methods for ICP-OES analysis of a wide range of analytes in heavy metal contaminated soil samples with specific reference to arsenic and antimony.” In: *Communications in soil science and plant analysis* 35.9-10 (2004), pp. 1369–1385.
- [48] Celio Pasquini et al. “Laser induced breakdown spectroscopy.” In: *Journal of the Brazilian Chemical Society* 18 (2007), pp. 463–512.
- [49] David A Cremers and Leon J Radziemski. *Handbook of laser-induced breakdown spectroscopy*. John Wiley & Sons, 2013.

- [50] Evgeniya Paulis. “Laser-induced breakdown spectroscopy of copper, nickel and nickel-phosphorus coatings: influence of laser wavelength.” PhD thesis. Wien, 2017.
- [51] Oleg L Antipov, ON Ereimeikin, and Aleksandr Pavlovich Savikin. “Spectroscopic studies of the population of high-energy levels of Nd³⁺-doped laser crystals upon intense pumping.” In: *Quantum Electronics* 32.9 (2002), p. 793.
- [52] Xiaoping Guo et al. “Diode-pumped 1123-nm Nd: YAG laser.” In: *Chinese Optics Letters* 2.7 (2004), pp. 402–404.
- [53] URL: <https://www.olympus-lifescience.com/en/microscope-resource/primer/techniques/confocal/pmtintro/>.
- [54] <https://sciencesprings.wordpress.com/2018/05/22/from-astrobiters-new-frontiers-in-ccd-systematics/ccd-schematic/>.
- [55] Michael Gaft et al. “Review on recent advances in analytical applications of molecular emission and modelling.” In: *Spectrochimica Acta Part B: Atomic Spectroscopy* (2020), p. 105989.
- [56] Jens Hildenhagen and Klaus Dickmann. “Nd:YAG laser with wavelengths from IR to UV (ω , 2ω , 3ω , 4ω) and corresponding applications in conservation of various artworks.” In: *Journal of Cultural Heritage* 4 (2003). Lases in the Conservation of Artworks - LACONA IV, pp. 174–178. ISSN: 1296-2074. DOI: [https://doi.org/10.1016/S1296-2074\(02\)01194-9](https://doi.org/10.1016/S1296-2074(02)01194-9). URL: <https://www.sciencedirect.com/science/article/pii/S1296207402011949>.
- [57] Marcel Guillong, Ingo Horn, and Detlef Günther. “A comparison of 266 nm, 213 nm and 193 nm produced from a single solid state Nd: YAG laser for laser ablation ICP-MS.” In: *Journal of analytical atomic spectrometry* 18.10 (2003), pp. 1224–1230.
- [58] Nazar Farid et al. “Laser-induced breakdown spectroscopic characterization of tungsten plasma using the first, second, and third harmonics of an Nd: YAG laser.” In: *Journal of Nuclear Materials* 433.1-3 (2013), pp. 80–85.

- [59] Tetsuhiko Matsuda, Shunsuke Kashiwakura, and Kazuaki Wagatsuma. “Statistical analysis on the distribution of alumina inclusion particles in ferritic stainless steels in laser-induced breakdown spectrometry using 1-kHz Q-switched Nd: YAG laser.” In: *Microchemical Journal* 153 (2020), p. 104400.
- [60] Josef Felver et al. “High-energy laser pulses for extended duration megahertz-rate flow diagnostics.” In: *Optics Letters* 45.16 (2020), pp. 4583–4586.
- [61] S Rosenwasser et al. “Development of a method for automated quantitative analysis of ores using LIBS.” In: *Spectrochimica Acta Part B: Atomic Spectroscopy* 56.6 (2001), pp. 707–714.